Correction published 18 November 2003

An intercomparison of lidar-derived aerosol optical properties with airborne measurements near Tokyo during ACE-Asia

Toshiyuki Murayama,[1] Sarah J. Masonis,[2] Jens Redemann,[3] Theodore L. Anderson,[2] Beat Schmid,[3] John M. Livingston,[4] Philip B. Russell,[5] Barry Huebert,[6] Steven G. Howell,[6] Cameron S. McNaughton,[6] Antony Clarke,[6] Makoto Abo,[7] Atsushi Shimizu,[8] Nobuo Sugimoto,[8] Masanori Yabuki,[9,10] Hiroaki Kuze,[9] Shunsuke Fukagawa,[9] Kari Maxwell-Meier,[11] Rodney J. Weber,[11] Douglas A. Orsini,[11] Byron Blomquist,[6] Alan Bandy,[12] and Donald Thornton[12]

[1]   During the ACE-Asia intensive observation period (IOP), an intercomparison experiment with ground-based lidars and aircraft observations was conducted near Tokyo. On 23 April 2001, four Mie backscatter lidars were simultaneously operated in the Tokyo region, while the National Center for Atmospheric Research C-130 aircraft flew a stepped-ascent profile between the surface and 6 km over Sagami Bay southwest of Tokyo. The C-130 observation package included a tracking Sun photometer and in situ packages measuring aerosol optical properties, aerosol size distribution, aerosol ionic composition, and SO_2 concentration. The three polarization lidars suggested that the observed modest concentrations of Asian dust in the free troposphere extended up to an altitude of 8 km. We found a good agreement in the backscattering coefficient at 532 nm among lidars and in situ 180° backscatter nephelometer observations. The intercomparison indicated that the aerosol layer between 1.6 and 3.5 km was a remarkably stable and homogenous in mesoscale. We also found reasonable agreement between the aerosol extinction coefficients ($\sigma_a \sim 0.03$ km^{-1}) derived from the airborne tracking Sun photometer, in situ optical instruments, and those estimated from the lidars above the planetary boundary layer (PBL). We also found considerable vertical variation of the aerosol depolarization ratio (δ_a) and a negative correlation between δ_a and the backscattering coefficient (δ_a) below 3.5 km. Airborne measurements of size-dependent optical parameters (e.g., the fine mode fraction of scattering) and of aerosol ionic compositions suggests that the mixing ratio of the accumulation-mode and coarse-mode (dust) aerosols was primarily responsible for the observed variation of δ_a. Aerosol observations during the intercomparison period captured the following three types of layers in the atmosphere: a PBL (surface to 1.2–1.5 km) where fine (mainly sulfate) particles with a low δ_a (<10%) dominated; an intermediate layer (between the top of the PBL and 3.5 km) where fine particles and dust particles were moderately externally mixed, giving moderate δ_a; and an upper layer (above ~3.5 km) where dust dominated, giving a high δ_a (30%). A substantial dust layer between 4.5 and 6.5 km was observed just west of Japan by the airborne instruments and found to have a lidar ratio of 50.4 ± 9.4 sr. This agrees well with nighttime Raman lidar measurements made later on this same dust layer as it passed over Tokyo, which found a lidar ratio of 46.5 ± 10.5 sr.   *INDEX TERMS:* 0305 Atmospheric Composition and Structure: Aerosols and particles

[1]Tokyo University of Mercantile Marine, Tokyo, Japan.
[2]Department of Atmospheric Sciences, University of Washington, Seattle, Washington, USA.
[3]Bay Area Environmental Research Institute, Sonoma, California, USA.
[4]SRI International, Menlo Park, California, USA.
[5]NASA Ames Research Center, Moffett Field, California, USA.
[6]Department of Oceanography, University of Hawaii, Honolulu, Hawaii, USA.

[7]Department of Electrical Engineering, Tokyo Metropolitan University, Hachioji, Tokyo, Japan.
[8]Atmospheric Environment Division, National Institute of Environmental Studies, Tsukuba, Japan.
[9]Center for Environmental Remote Sensing, Chiba University, Chiba, Japan.
[10]Now at National Institute of Polar Research, Tokyo, Japan.
[11]School of Earth and Atmospheric Sciences, Georgia Institute of Technology, Atlanta, Georgia, USA.
[12]Department of Chemistry, Drexel University, Philadelphia, Pennsylvania, USA.

1. Introduction

[2] It is widely recognized that tropospheric aerosols play an important role in Earth's radiation budget through the scattering and absorption of sun and earth radiation [e.g., *Charlson et al.*, 1992; *Hansen et al.*, 1997]. However, tropospheric aerosols are highly variable in time and space due to nonuniform source distributions and the strong influence of meteorological conditions on aerosol concentration and characteristics. The types of aerosols are dependent on their sources and regions, and can be categorized roughly as mineral dust, sea salt, volcanic, carbonaceous, or sulfate aerosols coming from various natural and anthropogenic origins. Uncertainty about the current level of radiative forcing due to these aerosols is relatively large compared to that of global warming gases [*Intergovernmental Panel on Climate Change (IPCC)*, 2001]. To improve forecasts of global climate change, it is necessary to reduce the uncertainties about aerosol effects.

[3] Recently, a number of large field campaigns have been conducted to characterize the physical and chemical properties of aerosols in selected regions, with a special focus on major aerosol outbreaks: for instance, TARFOX [*Russell et al.*, 1999], INDOEX [*Ramanathan et al.*, 2001], ACE-2 [*Raes et al.*, 1999], and LACE 98 [*Ansmann et al.*, 2002] aimed primarily at continental pollutions, SCAR-B [*Kaufman et al.*, 1998] and SAFARI [*Swap et al.*, 2002] aimed primarily at biomass-burning aerosol. Column closure studies coordinating airborne, satellite, and ground-based measurements are important in such large field campaigns in order to assess the accuracy of these observations and for constraining aerosol properties. Recently, such coordinated closure experiments have often included lidar observations [*Redemann et al.*, 1998, 2000; *Ferrare et al.*, 2000; *Welton et al.*, 2000; *Masonis et al.*, 2002; *Wandinger et al.*, 2002; *Fiebig et al.*, 2002].

[4] The Asian Pacific Regional Aerosol Characterization Experiment (ACE-Asia) was a large field campaign conducted under the auspices of the International Global Atmospheric Chemistry Program (IGAC). ACE-Asia focused on the outbreak of both mineral dust from the inner desert regions and anthropogenic aerosols from industrial areas in continental Asia and the Pacific region in the spring. Many coordinated physical and chemical observations of the aerosol, its evolution, and the radiative and climatic impacts were made across east Asia [*Huebert et al.*, 2003]. Under the framework of this campaign, intensive observations were carried out in April 2001 using ground-based instruments and the National Center for Atmospheric Research (NCAR) C-130 aircraft. This aircraft's flights were focused around Japan, Korea and the surrounding seas. Numerous ground-based observations were conducted simultaneously with these airborne measurements, involving a number of ground-based lidars. The

Mie polarization lidars were used to identify dust aerosol qualitatively at most of these lidar sites. This is because the large size and irregular shapes of dust aerosols cause higher values of linear depolarization ratio as compared with the accumulation-mode aerosols [*Iwasaka et al.*, 1988; *Murayama et al.*, 2001a; *Sassen*, 1999].

[5] Methods proposed by *Fernald* [1984] and *Klett* [1985] have been widely used for retrieving aerosol backscattering (or extinction) coefficients from the Mie backscatter lidar signal. In these algorithms, it is necessary to assume a boundary condition at the far end (normally at a high, aerosol-free altitude where the lidar profile would match the profile expected from molecular Rayleigh scattering) and to assume a reasonably fixed value of the aerosol extinction-to-backscatter ratio (lidar ratio, S_a). However, the resulting extinction profiles depend strongly on the variability of S_a [e.g., *Sasano et al.*, 1985]. Currently, climatological values of the lidar ratio are being studied extensively as a function of aerosol type using either in situ measurements that separately determine aerosol extinction and 180° backscattering [*Doherty et al.*, 1999; *Anderson et al.*, 2000] or using advanced Raman lidars that can independently determine S_a [*Ferrare et al.*, 1998, 2001; *Ansmann et al.*, 2001; *Franke et al.*, 2001].

[6] To date, a few intercomparison studies between ground-based lidars and airborne measurements have been made in east Asia. Quantitative discussions on the optical properties of Asian dust related to lidar observations (e.g., the typical aerosol depolarization ratio and lidar ratio of dust, how dust mixes with fine (pollution) aerosol, how ambient humidity affects the dust) are rather scarce. The objectives of this paper are threefold: first, mesoscale inhomogeneity of aerosol assessed by simultaneous lidars and airborne measurements, second, an intercomparison of lidar-derived optical properties with airborne physical and chemical measurements, emphasizing on understanding and interpreting vertical variations, and third, a comparison of the optical properties for significant dust later as observed by Raman lidar and airborne measurements.

[7] During the ACE-Asia IOP, an intercomparison study between ground-based lidars and airborne measurements aboard the C-130 was conducted on 23 April 2001 in Tokyo region. Owing to strict air-traffic control in this region, the flight track was several tens of kilometers to 100 km distant from the lidar sites. Previous studies showed, however, that two lidars separated by about 60 km [the Tokyo University of Mercantile Marine (TUMM) lidar and the National Institute of Environmental Studies (NIES) lidar] exhibited very similar aerosol loading in the free troposphere [*Murayama et al.*, 2001a; *Liu et al.*, 2002]. Thus we expected to be able to have a meaningful intercomparison even under such poor collocation conditions, at least in the free troposphere where local aerosol emission does not have much influence. Taking advantage of the presence of several lidar sites in the area, data from four Mie backscatter lidars were analyzed with the
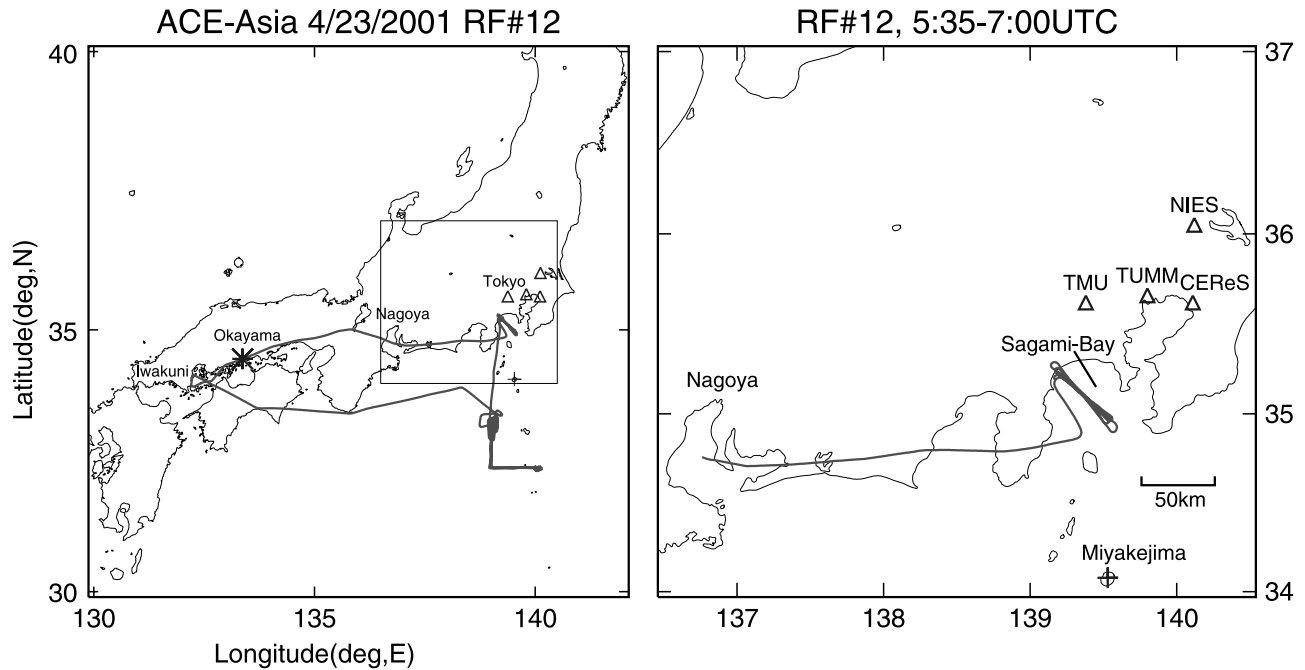
Figure 1. Flight track of the C-130 during the intercomparison on 23 April 2001 and location of the lidars. Curves indicate the flight track, and triangles and cross indicate the lidar sites and the Mt. Oyama volcano on Miyake-jima Island. The asterisk indicates the starting point of the descent explained in section 3.3.

simultaneously observed C-130 data. We also compared the TUMM Raman lidar observation with airborne observations for an elevated dense dust layer that appeared in later hours on the same day.

2. Observations and Results

2.1. Coordination of the Observation

[8] An intercomparison with lidar observations near Tokyo was conducted as part of the C-130's research flight (RF) 12 on 23 April 2001. During that period four institutes in the Tokyo region, TUMM (35.66°N, 139.80°N), NIES (36.05°N, 140.12°E), Tokyo Metropolitan University (TMU; 35.62°N, 139.38°E), and the Center for Environmental Remote Sensing (CEReS) of Chiba University (35.62°N, 140.11°E), operated their lidars simultaneously. Figures 1 and 2 show the flight track of the C-130 and the locations of the lidar sites.

[9] Before starting the lidar intercomparison flight legs, information from the TUMM lidar was relayed to the C-130 via the operation center at the Iwakuni base. Observing characteristic vertical structures in aerosol loading, several altitudes were selected for horizontal flight legs. On the basis of this information, the C-130 made a stacked, stair-type ascending with seven horizontal legs at about 0.15, 0.8, 1.8, 2.6, 3.6, 4.5 and 4.9 km altitudes over Sagami Bay northwest-to-southeast way from 0530–0625 UTC (Figures 1 and 2). Note that the local time is nine hours ahead of UTC. The 60 km-long horizontal legs were helpful for measuring the horizontal inhomogeneity of the aerosol and for estimating the extent to which the poor co-location of the platforms might be affecting the intercomparison.

[10] The C-130 flight track headed sharply away from the Tokyo region at 0625 UTC at ~4.9 km altitude, but continued to ascend to 7.6 km until 0700 UTC (Figure 2).

We included observations at the altitudes even above ~5 km in presented results, keeping in mind this poor collocation. Unfortunately, both the lidar and GMS-5 satellite indicated that thin cirrus clouds appeared over the Tokyo region during the intercomparison period. For the lidar analysis, we took account of the uncertainty caused by the cirrus clouds (section 2.2.3).

[11] Figure 3 depicts the meteorological data (air temperature, relative humidity, and wind direction and speed) measured from the C-130 during the intercomparison. The routine radiosonde observations at Tateno (36.05°N, 140.13°E) located near NIES on this day (1200 UTC) are also shown in the figure. We can clearly see inversion layers at about 1.2 and 3 km in both the C-130 and radiosonde data, indicating that the gross thermodynamic state of the atmosphere was similar in the two measurement regions.

2.2. Ground-Based Measurements

[12] All lidars included observations at 532-nm wavelength, and three of them (TUMM, TMU and NIES) measured the total depolarization ratio at 532 nm. Sun photometer observation was also simultaneously made at TUMM and CEReS. Here, we briefly mention the features of each lidar and Sun photometer, and present the retrieval methods used for the Mie polarization lidar. We describe individual lidar profiles during the intercomparison flight time period in section 2.2.3.

2.2.1. Lidars
2.2.1.1. Definition of Lidar Observable

[13] We will first introduce the quantities used for lidar. The backscattering ratio R at the altitude z is defined as

$$R(z) = \frac{\beta_m(z) + \beta_a(z)}{\beta_m(z)}, \tag{1}$$
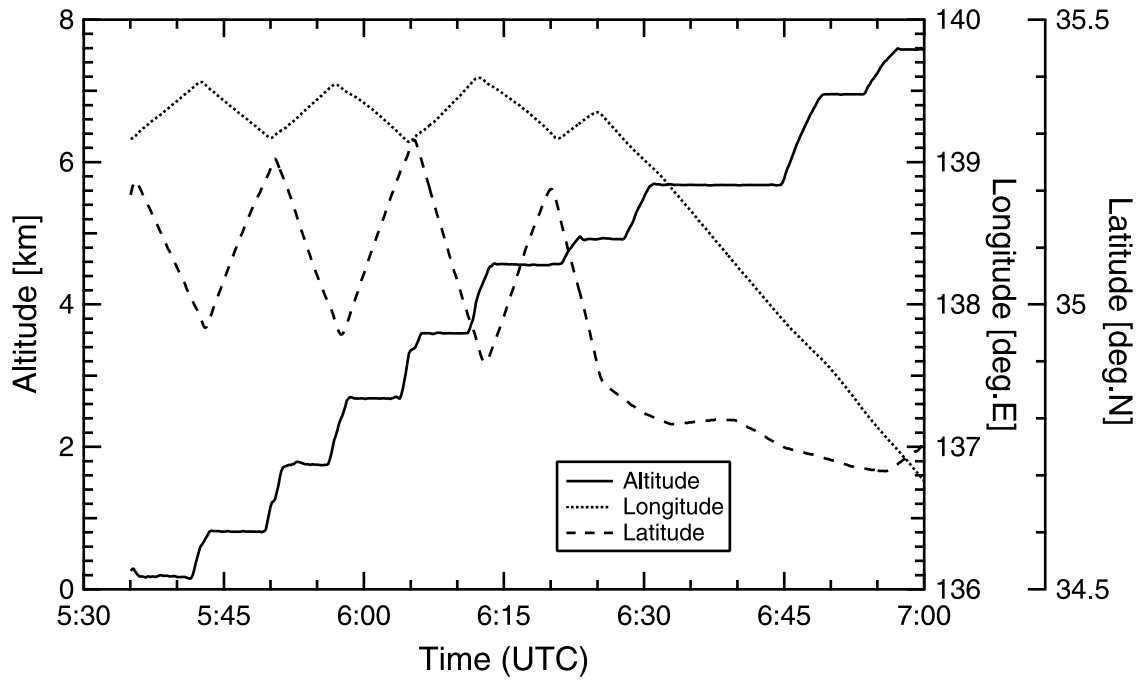
Figure 2. Variation of the altitude, longitude and latitude of the C-130 with time in the intercomparison. A stacked stair-type ascending profile with horizontal legs at several altitudes was made near Tokyo.

where β_m and β_a are the backscattering coefficients of air molecules and aerosols; β_m is evaluated using the atmospheric density given by local radiosonde observations or using a model atmosphere [*Measures*, 1984]. The extinction coefficients of air molecules and aerosols, σ_m and σ_a, are given by

$$\sigma_m(z) = \beta_m(z) \cdot S_m \qquad (2a)$$

$$\sigma_a(z) = \beta_a(z) \cdot S_a(z), \qquad (2b)$$
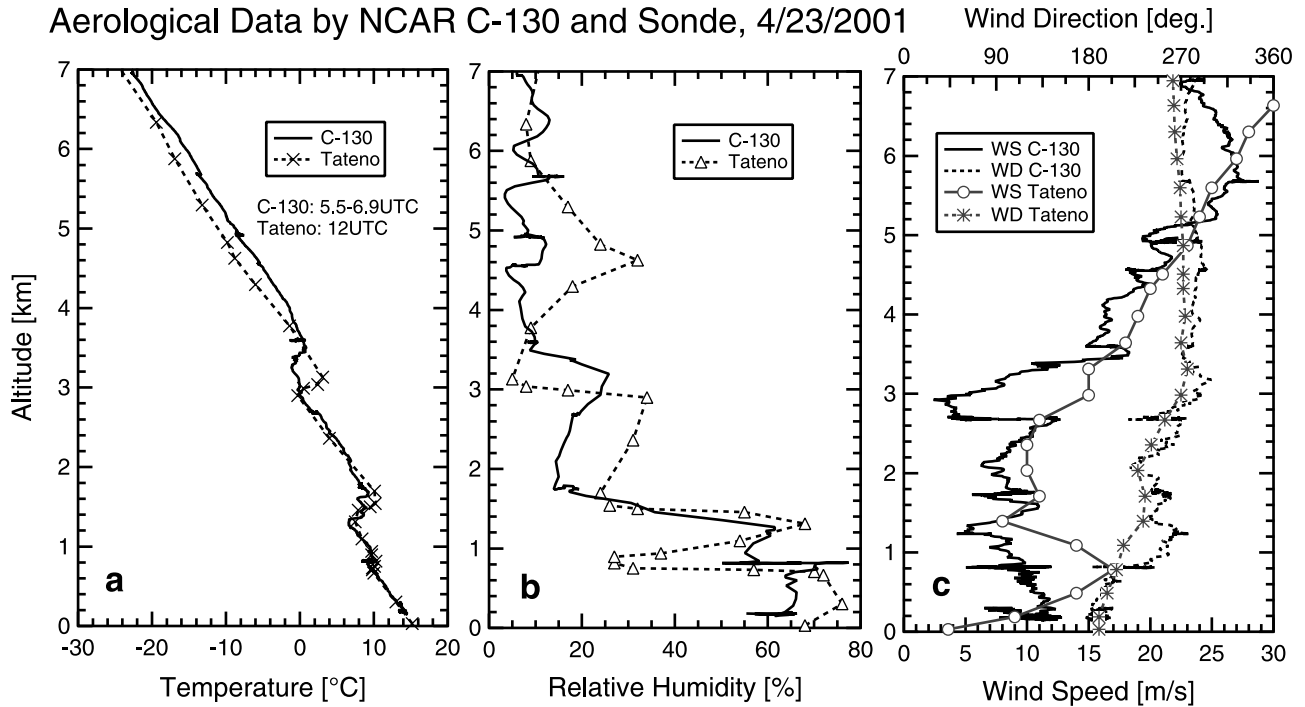
Figure 3. Meteorological data in the lidar intercomparison period (5.5–6.9 UTC) profiled by airborne sensors: (a) air temperature, (b) relative humidity, and (c) wind speed and direction. The radiosonde data at Tateno (36.05°N, 140.13°E) of this day (12 UTC) are also indicated.

where S_m and S_a are the extinction-to-backscatter ratio of air molecules and aerosols. For molecules, S_m is given by Rayleigh scattering theory as $8\pi/3$ [*Measures*, 1984]. In contrast, S_a (the lidar ratio) varies considerably depending on the aerosol size distribution, refractive index, shape of the aerosol particles, and the wavelength of incident light.

[14] We observe the polarization properties of the back-scattered light by separating the collimated light with a polarizing beamsplitter into the parallel and cross components of polarization. We define the following quantity as the total depolarization ratio (δ_t):

$$\delta_t(z) = \frac{P_\perp(z)}{P_{//}(z)} = \frac{\beta_{m,\perp}(z) + \beta_{a,\perp}(z)}{\beta_{m,//}(z) + \beta_{a,//}(z)}, \qquad (3)$$

where $P(z)$ is the Mie and Rayleigh backscattered signal at altitude z and subscripts $//$ and $\perp$ refer to the parallel and perpendicular components, with respect to the polarization plane of the emitted laser beam. The aerosol depolarization ratio $\delta_a (= \beta_{a,\perp}/\beta_{a,//})$ is derived from equations (1) and (3) as

$$\delta_a'(z) = \frac{\delta_t'(z) \cdot R(z) - \delta_m'}{R(z) - 1}, \qquad (4)$$

where $\delta_x' = \delta_x/(1 + \delta_x)$ ($x = m, a, t$), and $\delta_m (= \beta_{m,\perp}/\beta_{m,//})$ is the molecular depolarization ratio. The quantity δ_m depends on the wavelength and the bandwidth of the narrow interference filter used to suppress sky background light at the laser wavelength [*Adachi et al.*, 2001; *Behrendt and Nakamura*, 2002]. Although δ_a is directly related to aerosol optical properties, the uncertainty of δ_a becomes large when the backscatter ratio R is close to unity. The aerosol depolarization ratio δ_a can be evaluated more accurately with a Raman lidar than a Mie lidar because the backscattering ratio is well retrieved with fewer assumptions [*Whiteman et al.*, 1992]. Raman lidar is also capable of deriving extinction and backscattering coefficients separately [*Ansmann et al.*, 1992].

2.2.1.2. Tokyo University of Mercantile Marine

[15] The lidar at TUMM is a combined Mie-Raman lidar with an Nd:YAG laser producing 532 nm and 1064 nm beams and multiple receivers sensing primary (Mie-Rayleigh scattered) and Raman-shifted backscatter [*Murayama et al.*, 1999]. During the measurements, the laser power per pulse was 20 mJ (daytime; Mie lidar mode) and 100 mJ (nighttime; Raman lidar mode) for the 532-nm beam and the repetition rate was 10 Hz. The backscattered light was collected with three telescopes 20, 25, and 30 cm in diameter and detected with photomulipler tubes (PMTs). The smaller two (near and far-field) receivers have cross polarization channels at 532 nm. We determined the overlap factor between the laser beam and receiver field-of-view (FOV) below 250 m by assuming a nearly constant extinction profile when retrieved backscattering profile was homogenous in the PBL on the preceding day. Raman backscattered light at 607 nm and 660 nm from nitrogen (N_2) and water vapor (H_2O) molecules, respectively, was collected by a third (largest) receiver and detected with a photon-counting method after separating dichroic mirrors and interference filters. We used 12-bit analog transient recorders (model TR40-160, Licel, Berlin, Germany) for

far-field receiver to improve the signal-to-noise ratio. The data was averaged for 5 min in the daytime and 7 min in the nighttime. The recording range resolution of 7.5 m was reduced to 30 m to improve the signal-to-noise ratio. Since we used an interference filter of 1-nm FWHM bandwidth in the receiver system, the expected δ_m is about 0.5% [*Behrendt and Nakamura*, 2002]. Additional instrumental bias in the observed total depolarization ratio δ_t, which is often caused from the incomplete separation of linear polarizations, etc. [*Biele et al.*, 2000], was estimated from adjusting δ_t at the aerosol-free region over 13 km to match with the expected δ_m value (0.5%) and it was subtracted from observed δ_t.

[16] The vertical distributions of aerosol and clouds by the lidar on that day are shown in Figure 4 as time-to-height indications (THIs) of the normalized backscattering, the total depolarization ratio, and the backscattering coefficient at 532 nm. The backscattering coefficient was evaluated by Fernald's method, assuming the backscattering ratio to be ~1.02 for altitudes higher than 9 km, and the constant lidar ratio of 45 sr, which is a representative value of column-averaged S_a on the observation day as described later. We used the atmospheric density profile from the radiosonde observation at Tateno. From the total depolarization ratio, we can infer a dust loading between 3 and 8 km, especially after 0800 UTC.

2.2.1.3. Tokyo Metropolitan University

[17] TMU also continuously operated a Mie polarization lidar at 532 nm on the intercomparison day. The output energy of the laser pulse was 50 mJ and the repetition rate was 10 Hz. The return light was collected by a telescope 20 cm in diameter with a FOV of 1 mrad, and was detected with PMTs. Data was acquired with a sampling rate corresponding to 15-m range and a time interval of 1 min. The backscattering ratio (backscattering coefficient) was derived using Fernald's method. The reference height was set at an altitude just above the mixed layer, and the boundary value of the backscattering coefficient was adjusted so that the profile would converge at high altitude. Here we used a constant S_a of 45 sr. The THIs of the backscattering ratio and the total depolarization ratio at 532 nm are shown in Figure 5, revealing an almost identical structure and evolution of aerosol loading to that seen in the TUMM polarization lidar data (Figure 4). A 2 to 3% offset is expected in the total depolarization ratio.

2.2.1.4. National Institute of Environmental Studies

[18] At NIES, a Mie lidar system with a compact Nd:YAG laser was assembled in a container equipped with a sealed glass window on the roof. This configuration allowed the lidar to be operated in an autonomous mode for long-term monitoring, regardless of the weather conditions (A. Shimizu et al., Continuous observations of Asian dust and other aerosols by polarization lidars in China and Japan during ACE-Asia, submitted to *Journal of Geophysical Research*, 2003). A laser pulse of 50 mJ at 532 nm was emitted vertically through the window at a 10 Hz pulse repetition rate. A 35 cm diameter telescope was employed as a receiver, and the collected light was detected with PMTs. The retrieved signals were averaged for 5 min with 10-min intermissions, producing a 15-min repetition cycle. Fernald's method was also employed to calculate backscattering coefficients using S_a of 45 sr with an
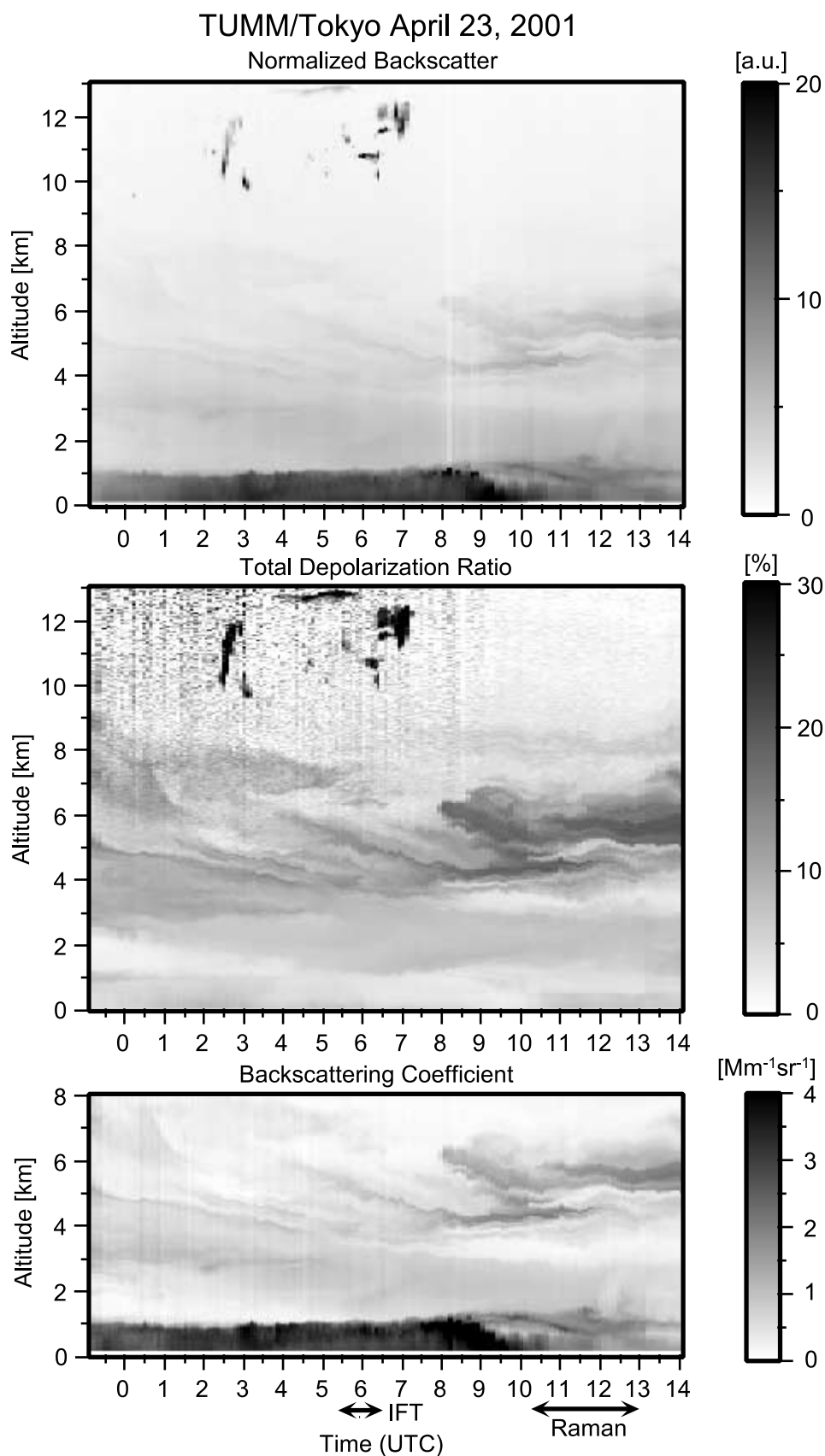
TUMM/Tokyo April 23, 2001

Figure 4. (top) Time-to-height indications of the normalized backscatter signal, (middle) the total depolarization ratio, and (bottom) the backscattering coefficient at 532 nm in TUMM on 23 April 2001. Arrows indicates the time period of the intercomparison flight and Raman-lidar mode observations. See color version of this figure at back of this issue.
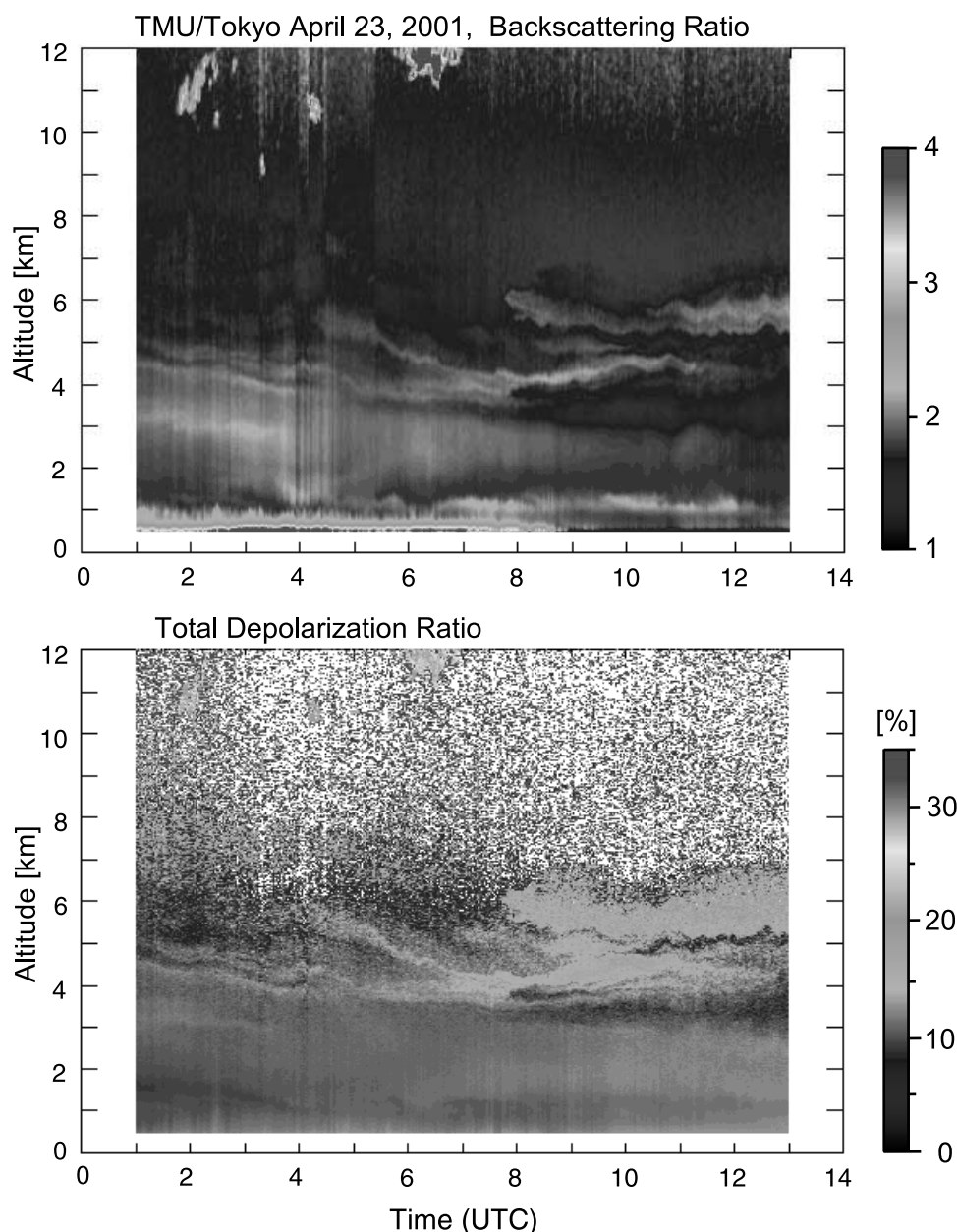
Figure 5. (top) THIs of the backscattering ratio and (bottom) the total depolarization ratio at 532 nm in TMU on 23 April 2001. Although TMU locates about 50 km west of TUMM, the both data agree well each other except in the boundary layer. See color version of this figure at back of this issue.

atmospheric density profile given by the U.S. Standard Atmosphere (US GPO, Washington, DC, 1976).

2.2.1.5. Center for Environmental Remote Sensing, Chiba University

[19] A multiple-wavelength, Mie scattering lidar based on a Nd:YAG laser and a Ti:Sapphire laser was operated at CEReS, Chiba University [*Kinjo et al.*, 2001]. Only the 532-nm lidar profile was analyzed due to inadequate conditions for the other wavelengths. The output energy of the 532 nm laser was 100 mJ/pulse with a repetition rate of 10 Hz. An 80 cm diameter telescope was used to detect the backscattered signal. Fernald's method was applied with S_a set to 46.5 sr and by approximately assuming the boundary condition at 4.0 km.

2.2.2. Sun Photometers

[20] At TUMM, a portable Sun photometer (model MS-120, EKO, Tokyo, Japan) with observation wavelengths of 368, 500, 675 and 778 nm was manually operated. The absolute calibration of the Sun photometer was performed at CEReS soon after the ACE-Asia IOP by comparison with a grating Sun photometer (model PGS-100, Prede, Tokyo, Japan) that is calibrated annually at the high-altitude Mauna Loa Observatory (MLO) in Hawaii. At TUMM, we also simultaneously employed a sun/sky radiometer (model POM-01, Prede) [*Murayama et al.*, 2001a]. The apparatus is similar to the CIMEL Sun photometer that has been widely used in the Aerosol Robotic Network (AERONET) [*Holben et al.*, 1998]. POM-01 has aerosol channels at 400,
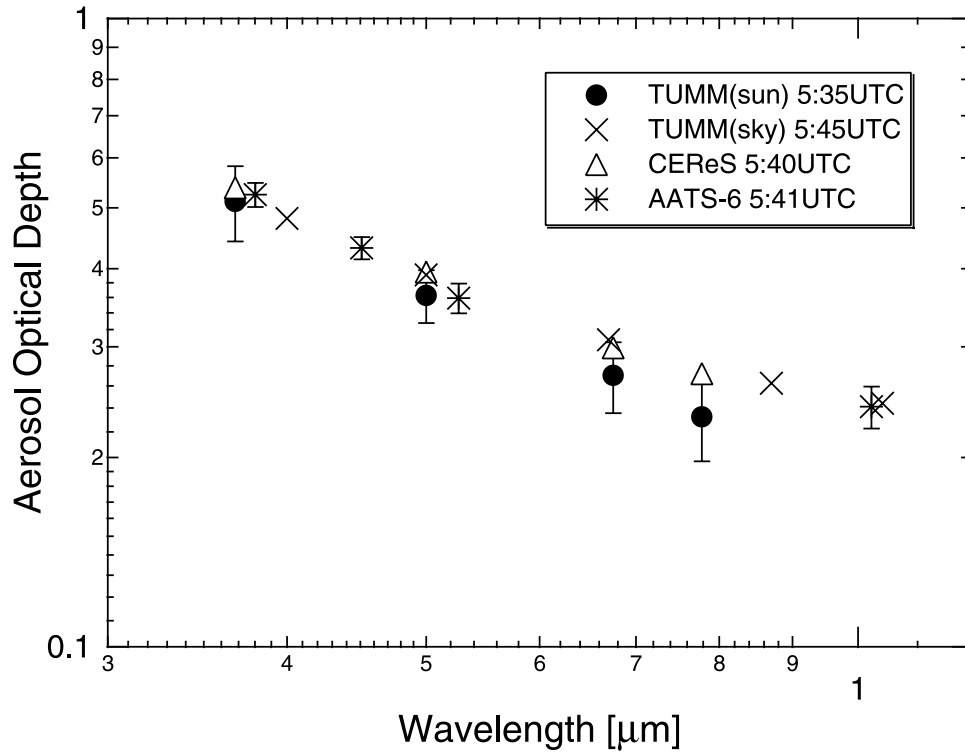
Figure 6. Wavelength dependence of aerosol optical thickness obtained by the Sun photometers and sky radiometer at TUMM and CEReS during the intercomparison. The data obtained by the airborne tracking Sun photometer, AATS-6, near the surface are also indicated for the comparison.

500, 670, 870 and 1040 nm. The aerosol optical depth (AOD) was retrieved from the skyradiometer data using program codes developed by *Nakajima et al.* [1996].

[21] AOD has been measured at CEReS, Chiba University since December 1999, using a Sun photometer (model PSF-100, Prede) operated at wavelengths of 368, 500, 675, and 778 nm. The data were acquired every 10 s. The wavelength dependence of AOD (τ_a) is often characterized by the following empirical equation [*Ångström*, 1929]:

$$\tau_a(\lambda) = \beta\lambda^{-a}, \tag{5}$$

where λ is the wavelength in microns, β is Ångström's turbidity coefficient corresponding to τ_a at $\lambda = 1$ μm and α is the Ångström exponent. This expression is useful for interpolating τ_a at observed wavelengths to other wavelengths. Figure 6 shows the observed AODs as a function of λ from the three ground-based Sun photometers and the airborne tracking Sun photometer aboard the C-130 during the intercomparison, and we see that the four data agree within instrumental errors.

2.2.3. Lidar Profiles During the Intercomparison

[22] It was no doubt desirable to match the lidar observation time to intercomparison flight time (IFT; 0530–0630 UTC), so that both aircraft and lidars observed the same air parcel. Unfortunately this was not allowed in the present intercomparison due to meteorological conditions: the wind direction over 1 km altitude was mostly westerly as shown in Figure 3, and the air parcel observed by the C-130 did not pass over the lidar sites. Therefore we simply compare the lidar profiles in the same period (0530–0630 UTC) with the

airborne measurements, assuming that the aerosol field was regionally uniform and rather horizontally homogenous. The validity of this assumption can be verified from the agreements among observed profiles, as described below.

[23] First we describe the estimation process of the column-averaged lidar ratio from the TUMM lidar and Sun photometer. The mean optical depth at 532 nm, as interpolated from Sun photometer data, was 0.347 ± 0.031 during the IFT (Figure 6). Considering the contribution of the thin cirrus clouds (Figures 4 and 5), we assumed the nominal AOD to be 0.31 ± 0.05. Furthermore, we assumed the backscattering ratio R at 9.67 km altitude to be 1.01 as the boundary condition, and then we applied Fernald's method iteratively to find lidar ratios that would give appropriate value of integrated AODs of 0.26, 0.31 and 0.36 [*Welton et al.*, 2000; *Kinjo et al.*, 2001]. Thus values of the lidar ratios S_a were determined as 35.6, 47.0 and 60.8 sr. The error of the backscatter coefficient due to the uncertainty of the lidar ratio is small at high altitudes but increases about ±10% below 3 km.

[24] The averaged profiles of the backscattering coefficients (four) and the total depolarization ratio (three) of the lidars during the IFT are indicated in Figure 7. The in situ backscattering coefficient measured by 180° backscatter nephelometer described later is also indicated. The indicated error bars of lidar profiles are taken from the standard deviations of several profiles during the IFT, which shows a measure of temporal fluctuation. We can see reasonable agreement in the backscattering profiles. The variability of aerosol loading with time and space is discussed in section 3.1. As seen in Figure 7, the values of the total

Tokyo Lidars/C-130 Intercomparison ACE-Asia RF12, 4/23/2001
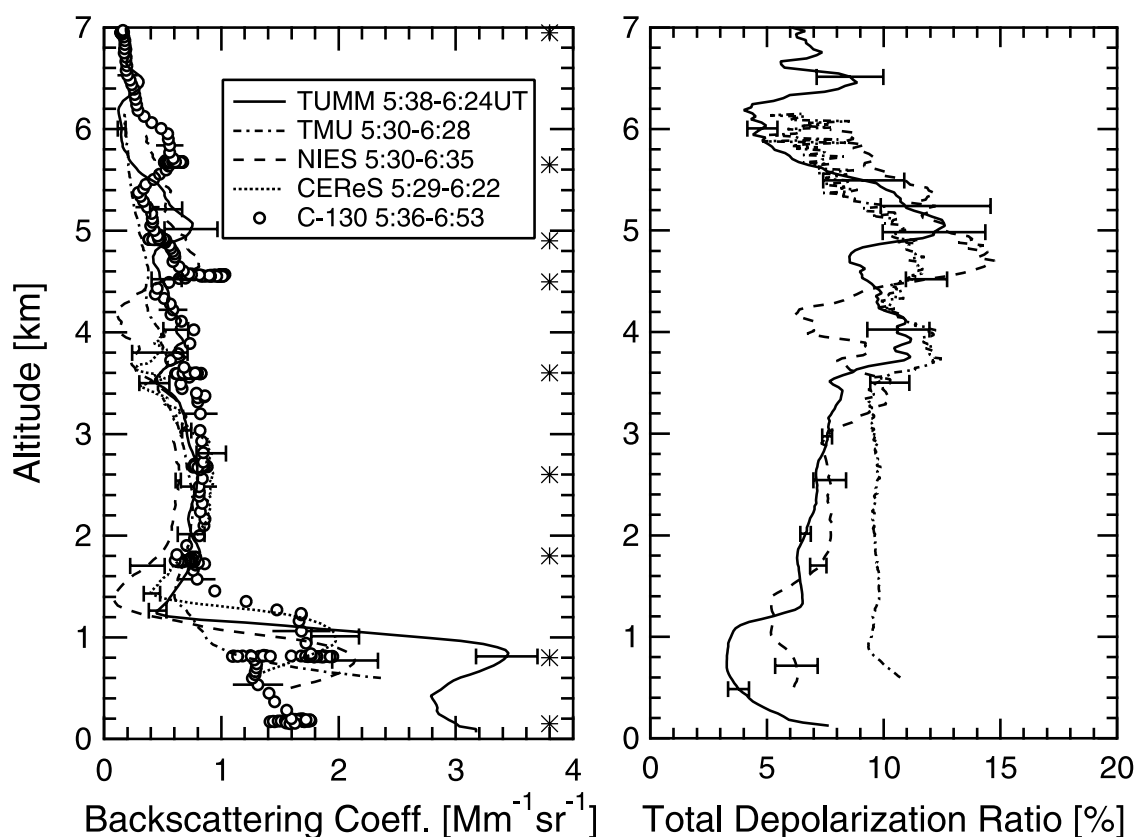
Figure 7. (left) Comparison of backscattering coefficients and (right) total depolarization ratios at 532 nm by the ground-based lidars in the Tokyo region during the intercomparison. In situ backscattering coefficients measured by the 180° backscatter nephelometer are also plotted. The asterisks indicated in the left figure show the heights of horizontal flight legs.

depolarization ratio δ_t above 3.5 km at TUMM, TMU, and NIES were as high as 10%, which suggests loading of Asian dust. The value of δ_t is correlated positively with the backscattering coefficient. This behavior is expected when the aerosol is nonspherical (dust-like; δ_a is high) and the backscattering ratio R is small (equation (4)). In contrast, as minutely but distinctly seen in TUMM lidar profiles, the correlation of β_a and δ_t was negative between 0.4 and 3.5 km. The oscillation seen in δ_t below 3.5 km is also found for the aerosol depolarization ratio δ_a in an enhanced way as described later.

2.3. Airborne Measurements

[25] For the analysis we have included the following C-130 based measurements: the optical data obtained by airborne in situ optical instruments (nephelometers and PSAP) and a tracking Sun photometer; the aerosol size distribution measured by an optical particle counter; the chemical measurements of water-soluble components; and the SO_2 concentration. In the following sections, we briefly describe the airborne instruments and give the results during the IFT.
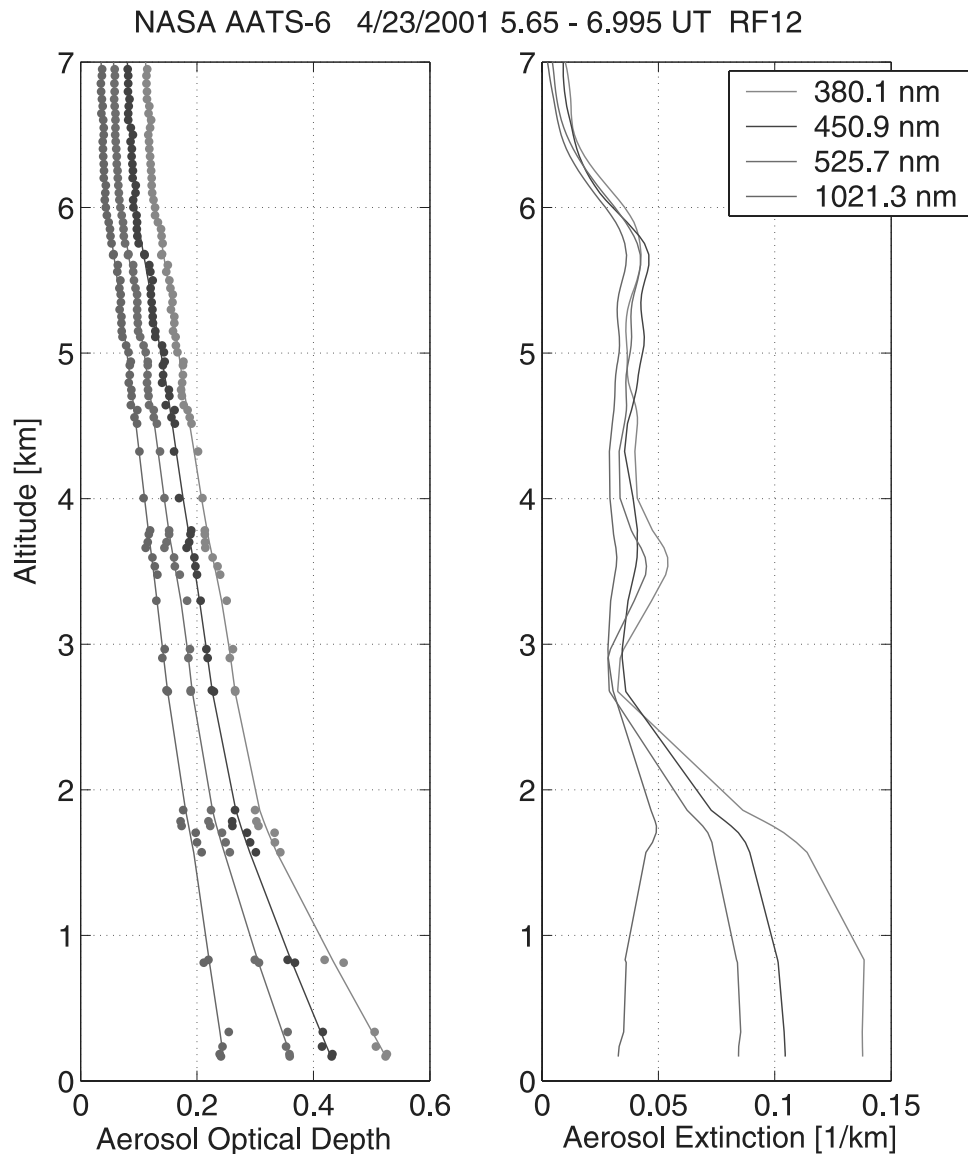
2.3.1. Tracking Sun Photometer

[26] In the spring 2001 phase of the ACE-Asia, the six-channel NASA Ames Airborne Tracking Sun photometer

(AATS-6) operated on 15 of the 19 research flights of the C-130. AATS-6 measures direct solar beam transmission at 6 wavelengths (380 to 1021 nm), yielding AOD spectra and column water vapor. Vertical differentiation of these data in suitable flight patterns yields extinction spectra and water vapor concentration.

[27] For the AATS-6, azimuth and elevation motors controlled by differential sun sensors rotate a tracking head so as to lock on to the solar beam and keep detectors normal to it. The tracking head of the instrument was mounted external to the aircraft skin to minimize blockage by aircraft structures and also to avoid data contamination by aircraft-window effects. Each channel consists of a baffled entrance path, interference filter, photodiode detector, and preamplifier, which are temperature-controlled to avoid thermally induced calibration changes.

[28] Premission and postmission radiometric calibration for the ACE-Asia field campaign was determined via Langley plots using data taken at the high-altitude MLO in March and June of 2001, respectively. For AATS-6, comparison of premission and postmission calibration constants, inspection of high-altitude AOD spectra, and in-flight and ground-based comparisons to AATS-14 revealed that premission calibration constants need to be used for all flights until 12 April 2001 (NCAR C-130 flights RF01–RF07); after that

Figure 8. (left) Observed vertical profiles of AOD spectra and (right) derived extinction coefficients by the airborne tracking Sun photometer AATS-6 during the intercomparison.

time, the postmission calibration is applied. Because of the occasional poor tracking performance of the AATS-6, a tracking uncertainty of 2% was added to the uncertainties in the calibration constants.

[29] Methods for AATS data reduction and error analysis can be found in the work of *Russell et al.* [1993] and *Schmid et al.* [2003]. Details that pertain to the analysis of AATS data obtained in ACE-Asia are described by *Redemann et al.* [2003]. The general procedure for deriving aerosol extinction profiles involves fitting the vertical AOD profiles with smoothed cubic spline functions, which are then differentiated with respect to altitude. The profiles of AOD spectra and thus derived extinction coefficients are shown in Figure 8. From the quality of the data, we believe that the AATS-6 data was almost free of contamination from thin cirrus clouds which appeared over the lidar sites during the IFT.

[30] While equation (5) describes the wavelength-dependence of AOD as a function of the Ångström coefficient, an analogous relationship exists for the wavelength-dependence of light extinction:

$$\sigma_a(\lambda) = \sigma_0 \lambda^{-k}. \tag{6}$$

Here we refer to k as the Ångström exponent on the extinction coefficient. The extinction profile of AATS-6 (Figure 8) indicates similar aerosol loading with the lidar observations (Figure 7). The derived Ångström exponent is indicated in Figure 9c with other data, which reveals a sharp contrast between in the free troposphere (small k; coarse-mode dominated) and in the PBL (large k; fine-mode dominated).

2.3.2. Nephelometers and PSAP

[31] Light scattering and absorption coefficients of both the total and fine mode (aerodynamic diameter, $D < 1\ \mu m$) aerosols were simultaneously measured by airborne TSI Inc. nephelometers at 450, 550 and 700 nm wavelengths and by

a Particle Soot Absorption Photometer (PSAP; Radiance Research, Seattle, WA) at 550 nm. A modified single-wavelength TSI Inc. nephelometer [*Doherty et al.*, 1999] was used to measure 180° backscattering of the total aerosol at 532 nm. All of these instruments operated at a low relative humidity (RH usually <∼45%). To provide information on aerosol hygroscopicity, a second pair of single-wavelength nephelometers (model M903, Radiance Research; 540 nm wavelength) was operated at low (<45%) and high (∼85%) RH. This two-point data set was used to derive the functional dependence of scattering on RH under the simple approximation that this function obeys an exponential form [*Kasten*, 1969]. These data are used here to adjust the measured total aerosol dry light scattering to ambient-RH light scattering. The dependence of light absorption on RH is not measured and so "ambient-RH" light extinction is calculated from ambient-RH light scattering and low-RH light absorption. This is not expected to lead to large error in our derived values of ambient-RH light extinction because absorption is such a small fraction (∼10%) of total extinction.

[32] All aerosols were sampled from the C-130 Low Turbulence Inlet (LTI) which is designed to admit very large ($D > 1\ \mu m$) aerosol [*Lafleur*, 1998]. Tests indicate that the sampling efficiency for the nephelometers and PSAP was ∼1.0 for aerosol of $D < 1\ \mu m$ but that there may have been enhancement in the coarse-mode ($D > 1\ \mu m$) scattering and absorption of ∼10% due to the LTI [*Anderson et al.*, 2003].

[33] The data processing procedure used to derive light scattering, absorption, and 180° backscatter from the in situ instruments is described in detail by *Anderson et al.* [2003]. Uncertainties associated with noise, calibration, correction factors, and RH adjustments have been determined (in most cases empirically) and these are propagated to provide the 95% confidence uncertainty on the derived quantities. Data were sampled either every 1 or 2 s but data presented here have been averaged to 10 s resolution, and then smoothed over a 30 second window to more closely match the vertical resolution of the lidars.

[34] In addition to measuring low-RH light scattering and absorption, 180° backscatter, and ambient-RH extinction, we were able to derive several quantities of relevance to this intercomparison, including: the lidar ratio, the Ångström exponent, the fine mode fraction (FMF) of light scattering (i.e., $D < 1\ \mu m$ scattering divided by total scatter), and the single scattering albedo (SSA) (Figure 9). All of these values are derived at low RH only; however, note that during the intercomparison the ambient RH itself was <40% for altitudes above ∼1.5 km (Figure 3b). Here we used the measured values of the Ångström exponent to adjust the values of light scattering at 450 and 550 nm to light scattering at 532 nm, so as to match the lidar and 180° backscatter nephelometer wavelengths. Light absorption is assumed to scale linearly with wavelength. This allowed us to calculate both light extinction and the lidar ratio at 532 nm. We also note that the plotted airborne in situ extinction data include all of the data from horizontal flight and that, indeed, the aerosol was rather horizontally homogeneous in the free troposphere. Figure 9 demonstrates that the extinction and Ångström exponent profiles agree reasonably well with those from the tracking Sun photometer.

2.3.3. Particle Sizer

[35] Aerosol particle size distributions from 0.12 to 15 μm were measured with a modified LAS-X optical particle counter (OPC). The optical systems were unchanged, but a custom-built log-amplifier and 256-channel pulse height analyzer were installed to enhance resolution. The OPC drew its air through the starboard LTI of the C-130. Samples were dried by mixing filtered and desiccated air into the sampling stream. No corrections for LTI enhancement and transport tubing losses have been incorporated since they appear to roughly cancel each other out.

[36] The OPC was calibrated before, during, and after the field project using latex (refractive index 1.58) and glass (refractive index 1.54) calibration spheres (Duke Scientific). No correction has been made here for the actual refractive index of the particles, so the diameters presented are best viewed as effective scattering diameters rather than geometric diameters. The vertical variation of the scattering size distribution and the normalized scattering coefficient in the horizontal legs are shown in Figure 10. The presentation by scattering coefficient, as opposed to the usual number or volume size distribution, makes it easy to see the relative influences of the accumulation mode and coarse particles on optical properties. We can clearly see the transition in the size distribution from the fine-mode dominated one in the PBL to the coarse-mode dominated pattern in the free troposphere.

2.3.4. Rapid Ion Chromatography

[37] Information on the chemical composition of the aerosols was useful in helping to test the relationship we expected between the aerosol optical properties and their composition. Aircraft measurements allow us to get vertically resolved information on ambient aerosol, but most chemical measurements of aerosol require sampling periods that are too long to be useful in profiles such as the one presented here. However, a recently developed instrument, the Rapid Ion Chromatograph (PILS-IC), capable of measuring relative abundances of water-soluble ions at a high sample rate, was deployed on the C-130 aircraft for ACE-Asia.

[38] Like the nephelometers and PSAP, this instrument drew its sample from the C-130 LTI. The sampled air was sent through denuders to remove interfering gas concentrations. The particles then mixed with saturated water vapor to form water droplets. The droplets grew in a particle growth chamber and collided with an impaction plate at the other end. The particles were collected from the plate with a collection fluid. The fluid containing the soluble ionic aerosol components was retrieved at the base of the plate. Air bubbles were removed and the collected sample fluid was divided and sent to two ion chromatographs to quantify their fine particle water-soluble ionic concentrations. The PILS-IC operated at a continuous, 4-min measurement cycle to detect: Na^+, NH_4^+, Ca^{2+}, Mg^{2+}, K^+, Cl^-, NO_3^-, and SO_4^{2-} [*Weber et al.*, 2001]. We performed laboratory studies using a Vibrating Orifice Aerosol Generator (VOAG) to estimate the collection efficiency versus diameter, we found that the collection efficiency was 50% at 1.3 μm. However, the samples retained a small portion of large particles (up to 3 μm), so collection was inefficiently. Measurement uncertainty is approximately ±30%.

[39] Figure 11 presents a vertical profile of the mass concentration of water-soluble components measured by
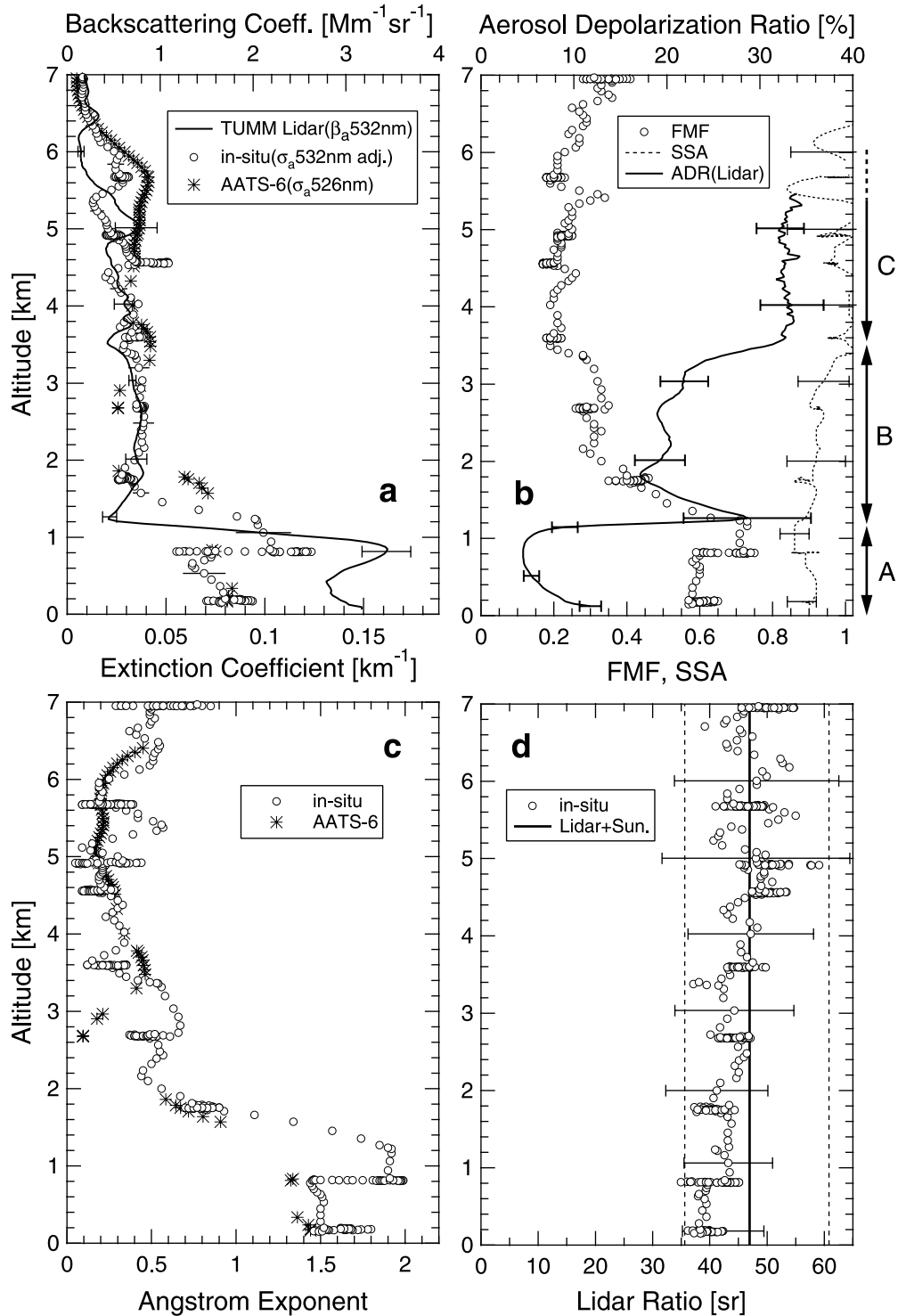
Figure 9. Vertical profiles of aerosol optical properties measured by airborne nephelometers and PSAP (in situ), tracking Sun photometer, and TUMM lidar during the intercomparison flight on 23 April 2001. (a) Extinction coefficient from in situ (adjusted at 532 nm) and AATS-6 (526 nm) measurements and backscattering coefficient from lidar (532 nm). (b) Fine mode fraction (FMF) of light scattering, single scattering albedo (SSA) from in situ measurements at 550 nm, and the aerosol depolarization ratio at 532 nm from the lidar. (c) Ångström exponent between 450 and 700 nm from in situ measurements and from the AATS-6. (d) Lidar ratio at 532 nm from in situ measurements and from the lidar-Sun photometer measurement at TUMM. Explanation of regions A, B, and C in Figure 9b are given in the text.
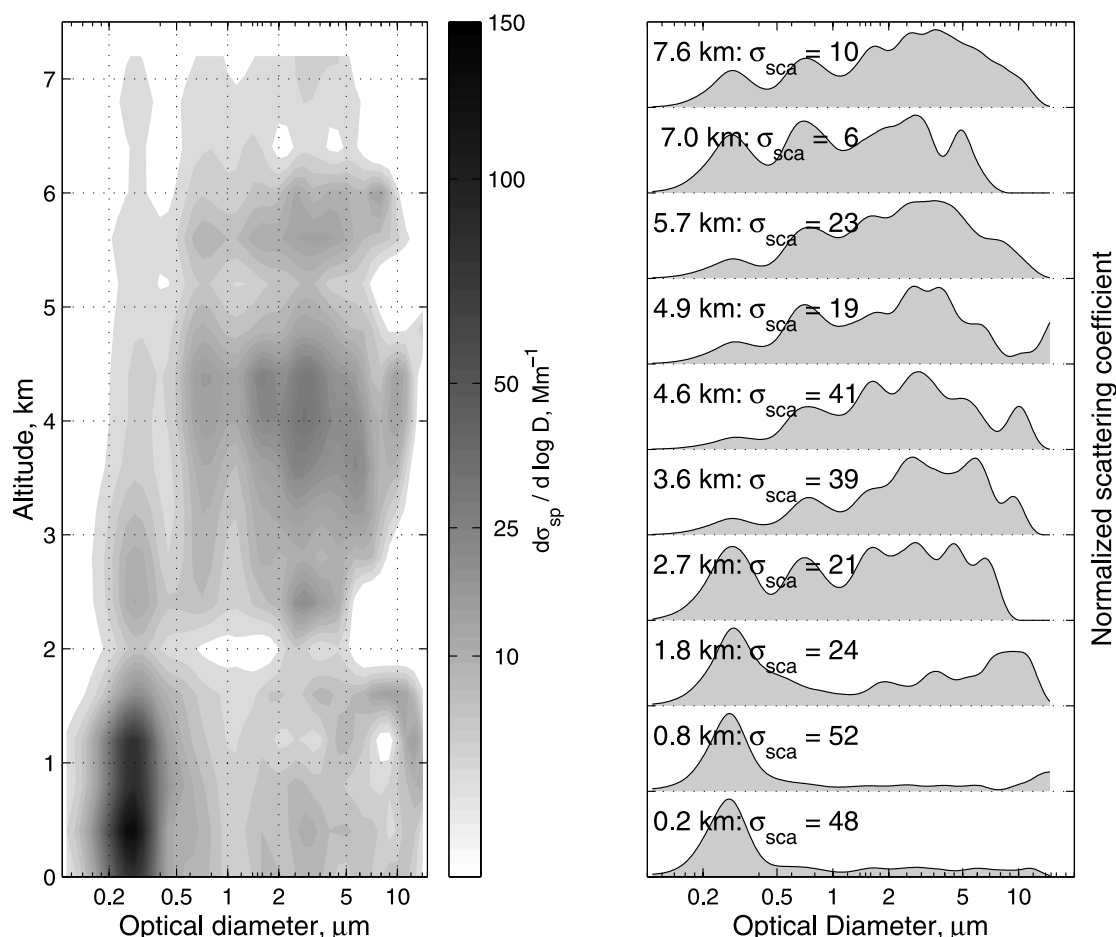
Figure 10. (left) The vertical variations of the scattering size distribution and (right) the normalized scattering size distribution averaged in the horizontal legs.

the PILS-IC and the vertical variation of the ion equivalent ratios, which are normalized by the sum of detectable equivalents. A high concentration of sulfate was observed below 1.5 km, and a sharp relative increase of Ca^{2+} (considered to be a good indicator of mineral dust), above 3 km. However, we note that we analyzed only the water-soluble components of fine particles (diameter <3 μm) here and that only a small fraction of the total calcium in dust is soluble.

2.3.5. SO$_2$ Measurement

[40] Fast sulfur dioxide measurements were obtained on board the C-130 with a newly developed Atmospheric Pressure Ionization Mass Spectrometer (APIMS) [*Thornton et al.*, 2002]. This instrument uses an isotopic internal standard (^{34}S labeled SO$_2$) to achieve continuous in-flight calibration. The measurement relies on the reaction of SO$_2$ with CO_3^- ions (produced at atmospheric pressure in a ^{63}Ni radioactive source) and molecular oxygen to produce SO_5^-. These ions, from both ambient air and the internal standard, are detected by the mass spectrometer at masses 112 ($^{32}SO_5^-$) and 114 ($^{34}SO_5^-$). The concentration of ambient SO$_2$ is calculated from the signal ratio of mass 112 to mass 114 and the known concentrations of labeled internal standard added continuously to the ambient air. For ACE-Asia data were recorded at approximately 2 Hz and then

averaged to 1 Hz for the results presented here. The detection limit at this data rate was 5 pptv.

[41] Figure 12 illustrates the profile of SO$_2$ concentration from the intercomparison period with water vapor mixing ratio. An elevated SO$_2$ plume at 10 ppb level was observed between 0.8 and 1.5 km. This might have originated from the Mt. Oyama volcano on Miyake-jima Island (Figure 1) and/or urban plumes as discussed later. A high concentration near the surface may be due to pollution from nearest coastal area.

3. Discussion

### 3.1. Mesoscale Variability of Aerosol Assessed by Simultaneous Lidars and Airborne Observations

[42] As seen from the backscatter intercomparison indicated in Figure 7, we can recognize an extremely stable and horizontally homogeneous aerosol layer between 1.6 km and 3.5 km. We note that all observations were made in an about 150 km circle and in about one hour. Below about 1.6 km and above 3.5 km the variability among the observations is higher, which is also indicated by individual observation: relatively higher variability in in situ measurement of 60 km horizontal legs at 0.15, 0.8 and 4.5 km, and relatively higher standard deviations (error bars) of the
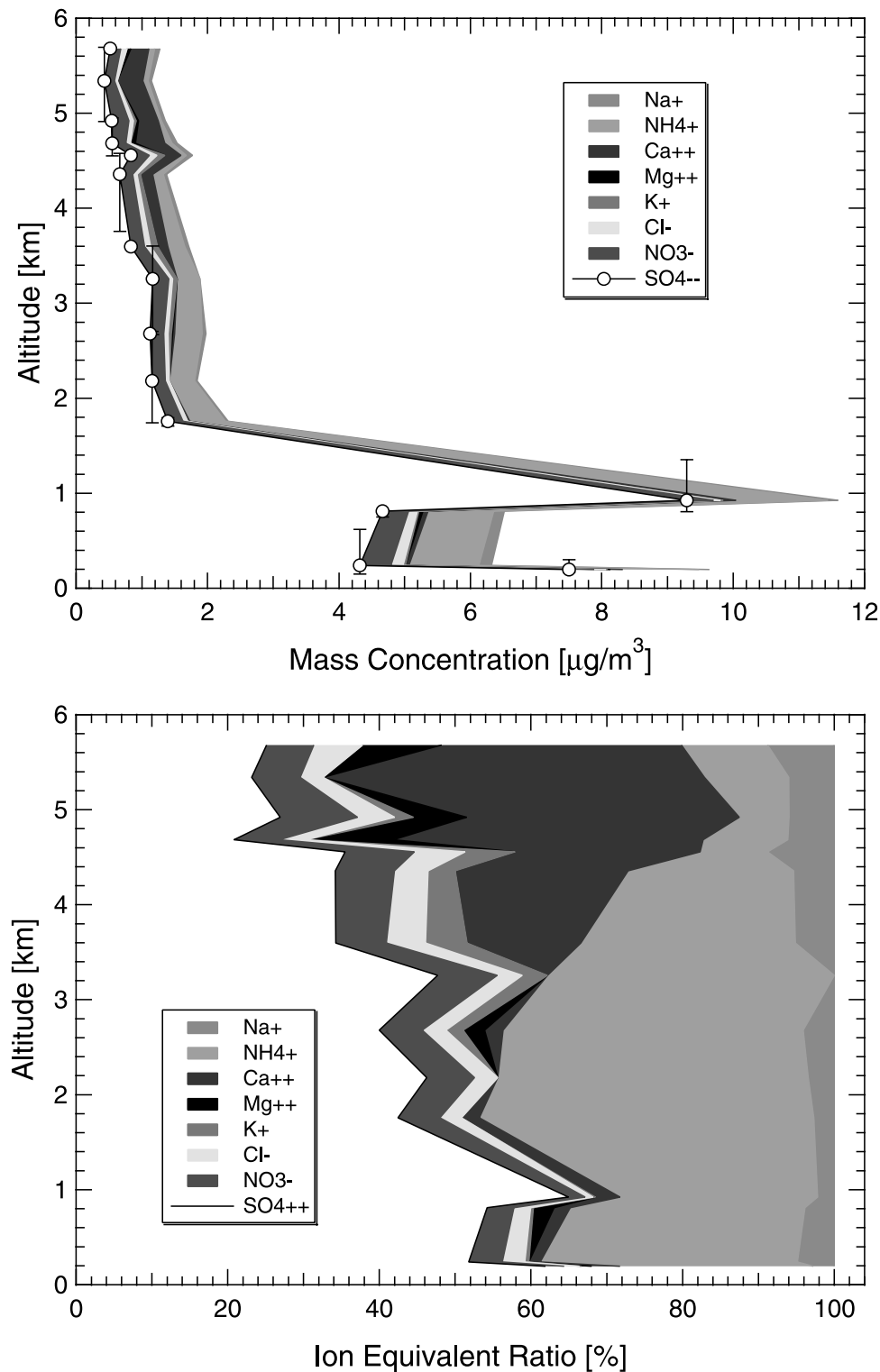
Figure 11. (top) Vertical variation of the mass concentration and (bottom) the ion equivalent ratio of water-soluble species in fine aerosols (diameter <3 μm). The left-most white portions indicate those of sulfate. Open circles and error bars for sulfate in the top panel indicate the midaltitude and height range of each sample.

backscattering coefficients from the lidars. High variability below 1.6 km could be caused by the difference of PBL height and local surface influence. A higher local aerosol loading at TUMM in the PBL is expected than at the other sites because TUMM is located in the most central area of Tokyo. The variability above 3.5 km might be caused by wind sheer due to gravity waves, which was recognized as wavy structure of upper aerosol layers in THIs of lidar
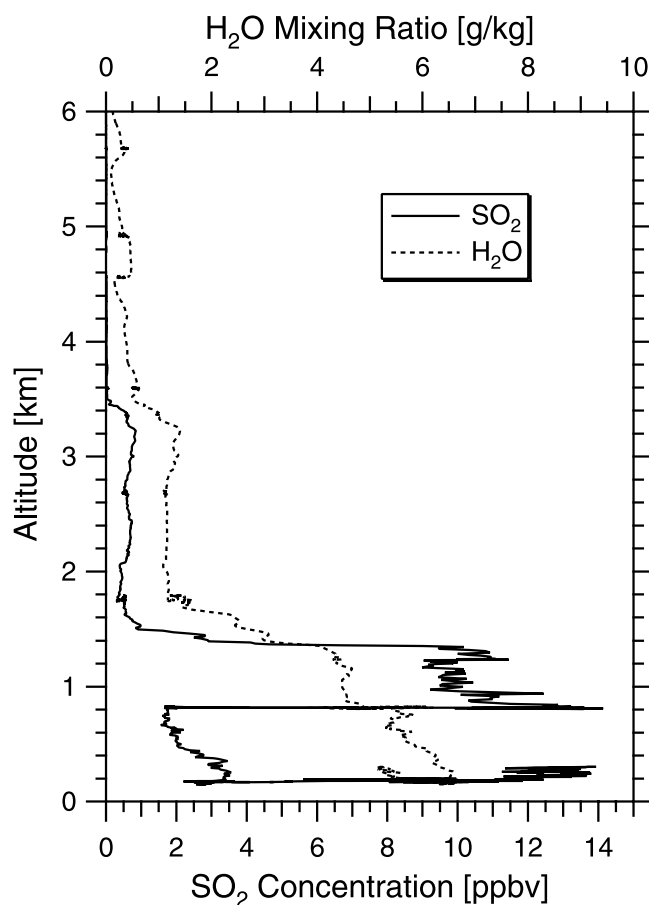
Figure 12. Vertical profile of SO_2 concentration during the intercomparison. Water vapor mixing ratio is also indicated.

backscatters (Figures 4 and 5). The remarkable stability in the intermediate layer allows us a closer intercomparison described in the following section.

3.2. Vertical Variation of Aerosol Optical and Chemical Properties During the IFT

[43] Here we compare the aerosol optical properties from the TUMM lidar (as a representative of ground-based lidar data) with those obtained from the airborne measurements and discuss what collective data sets tell us about the aerosol in the region. Figure 9 depicts vertical profiles derived from the AATS-6 Sun photometer, the in situ optical instruments on board the C-130, and the TUMM lidar. The axis of β_a (upper axis of Figure 9a) is determined by scaling to the axis of σ_a (lower axis of Figure 9a) by using an assumed value of $S_a = 47$ sr. The error indicated in the backscattering coefficient by the TUMM lidar in Figure 9a represents the temporal fluctuation of the backscattering coefficient (section 2.2.3). The error associated with the extinction coefficient should be linearly magnified by the uncertainty of S_a. Above the boundary layer ($>\sim 1.8$ km), the extinction profile in this way agrees fairly well with airborne measurements: all the three profiles follow nearly the same mean extinction level (~ 0.03 km^{-1} between 2 and 5 km) and they exhibit similar magnitudes of variability. The disagreement below 1.8 km can be ascribed plausibly to the difference of the PBL height, which was higher over the ocean than over the land. Other possible but less certain

causes are more aerosol loading in downtown Tokyo than over the ocean (section 3.1), and an incorrect assumption of the lidar ratio in the PBL.

[44] In Figures 9a and 9b a notable relationship is seen between the altitude dependence of the backscattering coefficient β_a and that of the aerosol depolarization ratio δ_a. A distinct negative correlation is found between β_a and δ_a between 0.4 and 3.5 km, but δ_a was nearly constant while β_a changes above 3.5 km. Similar correlation behavior of backscatter and depolarization during Asian dust events was reported by *Murayama et al.* [2001a, 2001b]. Using aerosol depolarization data, we can break the profile down into three vertical ranges as indicated in Figure 9b as region A ($z < 1.2$ km) where β_a is high and δ_a is low ($<10\%$); region B ($1.2 \text{ km} < z < 3.5 \text{ km}$) where δ_a is at midrange and is negatively correlated with β_a, which is low; and region C ($z > 3.5$ km) where δ_a is high ($\sim 30\%$) and almost constant with altitude, and β_a is low. These characteristics can be explained by the mixing ratio of fine (accumulation-mode) and dust (coarse-mode) aerosols. Fine aerosols do not cause a significant depolarization at 532 nm even if they are nonspherical [*Mishchenko and Sassen*, 1998; *Murayama et al.*, 1999]. In contrast, the dust particles cause a high degree of depolarization due to their large size and irregular shapes. Given that fine aerosols and dust aerosols are externally mixed so as to cause a moderate depolarization, the increase of fine-mode particle scattering raises the backscattering coefficient but lowers the depolarization ratio, leading to the observed negative correlation between δ_a and β_a.

[45] This characterization of the aerosol properties, based on the Mie polarization lidar data at 532 nm alone, is also supported by airborne physical and chemical measurements. As shown in Figure 9b, the FMF of the scattering coefficient at 550 nm was as small as 0.2 above 3.5 km, indicating dominance of dust aerosol. It then gradually increased with decreasing altitude between 3.5 and 1.2 km, where the lidar data showed a drastic change in δ_a. Below this range, FMF remains high, especially in the dense aerosol layer between ~ 1.2 and 0.8 km, and δ_a remains low. The tendency was also seen in FMF was also seen in the Ångström exponents (Figure 9c), which is quite reasonable since both of these are size-dependent parameters.

[46] The size distribution measured by the airborne OPC (Figure 10) agrees well with the variation of FMF (Figure 9b). The aerosol single scattering albedo (Figure 9b), measured in situ from the C-130, also indicates three layers, with SSA 0.87 to 0.90 in region A, 0.96 in region C, gradually increasing with altitude from 0.88 to 0.96 in region B. It is likely that lower values of SSA are associated with pollution-related aerosols, and while higher values with Asian dust particles [*Anderson et al.*, 2003].

[47] The chemical data also reinforce our interpretation of the three aerosol layers. As shown in Figure 11, sulfate was dominant below 1.5 km and was moderately mixed with other species at higher altitudes. The dust component (Ca^{2+}) clearly increased above 3.5 km. We also see that the ion equivalence of SO_4^{2-} significantly exceeds that of NH_4^+ below 2 km. This indicates that the chemical form is not only $(NH_4)_2SO_4$ but also NH_4HSO_4 and H_2SO_4 at these levels. The high concentration of SO_4^{2-} also corresponds to the elevated SO_2 plume (~ 10 ppb) between 0.8 and 1.5 km (Figure 12). Therefore it is likely that the observed sulfate at

these altitudes was due to the fresh or diffused plume from the Mt. Oyama volcano on Miyake-jima Island, which was active at this time. On the other hand, an elevation of CO concentration is found in the same height range of the elevated SO_2 plume, which indicates urban plume signature (B. Blomquist, private communication, 2002). These facts suggest the mixture of volcanic and urban emissions. The concentration of SO_2 between 1.5 and 3.5 km was ~ 0.6 ppb and sharply decreased to zero over 3.5 km. The SO_2 concentration were well correlated with the water vapor mixing ratio in this height range, which might suggest regionally transported SO_2. It is also possible that some of the sulfate observed in the chemical data was transported from the continent to higher altitudes.

[48] While size-dependent optical properties and chemical composition of aerosol varies considerably as mentioned above, the in situ lidar ratio shows a small variation throughout the profiling. We note that in the PBL, the lidar ratio under ambient RH might differ from the in situ lidar ratio at low RH (<40%). The average value of in situ S_a between 0.18 and 5.9 km was 44.9 ± 10.9 sr. This value agrees well with the column-averaged S_a ($47.0 + 12.5 - 13.8$ sr) derived from observations of lidar and Sun photometer (section 2.2.3). The fact that the profile of in situ lidar ratio was less height-dependent coincides with the findings by *Anderson et al.* [2003]. They reported that values of S_a at low RH were 50 ± 5 sr for fine-dominated samples and 46 ± 8 sr for coarse-dominated samples during the ACE-Asia IOP. The nonsphericity of dust certainly raises the lidar ratio higher than the value (~ 20 sr) expected from Mie theory [*Liu et al.*, 2002; *Ackermann*, 1998], which might contribute to the small variation in the lidar ratio in this region.

3.3. Raman Lidar Observation and Aircraft Observations for Elevated Dust Layer

[49] On the day of the intercomparison (23 April 2001), winds in the free troposphere were such that the C-130 and TUMM lidar probably sampled similar air masses when the aircraft was about 600 km west-southwest of Tokyo. This comparison is interesting because a very dense dust layer was observed from the C-130 on its descending flight into the Iwakuni base, starting when the aircraft was over Okayama (133.4°N, 34.5°E) indicated by the asterisk in Figure 1. This descent immediately followed the transit leg at about 7.5 km altitude after the intercomparison in Tokyo.

[50] The observations by the onboard nephelometers/PSAP and by the AATS-6 from 0732–0806 UTC are shown in Figure 13. We can clearly see a significant dust layer between 4 and 7 km. A corresponding Raman lidar observation was made from 1011–1302 UTC (see Figure 4). For the data shown in Figure 13, the C-130 and TUMM lidar were separated by about 600 km. Given the westerly wind speed of 20 to 30 m/s at 5 to 7 km altitude on this day (Figure 3c), we calculate that it took 5.5 to 8 hours for the air parcel to travel between Okayama and Tokyo. Therefore we believe that we observed nearly the same dust plume at both locations. Indeed, the Raman-lidar derived aerosol optical properties match those measured from the C-130 remarkably well (Figure 13).

[51] In the Raman lidar observations shown in Figure 13, the range resolution was reduced to 120 m, and a five-point sliding average was applied to the range-normalized signals

of Raman backscatter above 2 km in deriving the extinction profile. (The nominal height resolution was 600 m). The extinction coefficient using the Ångström exponent k measured by the nephelometer and AATS-6 (Figure 13c) to adjust for the difference between aerosol extinction at the incident laser wavelength (532 nm) and that at the return Raman-shifted wavelength by nitrogen molecules (607 nm). That is, we used $k = 0.1$ above 4 km and $k = 1.0$ below 2 km, and applied a linear interpolation for 2–4 km. The statistical errors expected from Poisson statistics were the main source of error in the extinction and lidar ratio profiles.

[52] Although the extinction coefficients derived from the Raman lidar are somewhat smaller than the C-130 observations, the agreement is quite good given the distance between the two observations. An even better agreement can be found if we focus on the aerosol optical property that does not depend on aerosol concentration. The averaged lidar ratio in the center of the dust layer, i.e., between 4.5 and 6.5 km, was 46.5 ± 10.5 sr according to the Raman observations. Here the mean value is obtained by simple averaging and the uncertainty is the standard deviation. The uncertainty thus includes the statistical measurement error and the actual change of the lidar ratio in the dust layer. The lidar ratio observed by the airborne in situ measurements was homogeneous in the dust layer as shown in Figure 13d; the mean value is 50.4 ± 9.4 sr. The in situ and Raman lidar measurements agree well within their uncertainty ranges. Comparison between δ_a and FMF (Figure 13b) suggests that δ_a is a strongly size-dependent parameter. The value of δ_a in the dust layer was about 30% at the maximum, which coincided with the estimate in the daytime observation (Figure 9b).

[53] *Sakai et al.* [2002] also performed Raman lidar observations at Nagoya (35.1°N, 137.0°E) and Tsukuba (36.1°N, 140.1°E) and observed similar elevated dust layers. They reported that the averaged value of S_a for the dust layer between 4 and 7 km observed at Tsukuba from 1040 to 1121 UTC was 46 ± 5 sr and that the maximum δ_a was about 30%, which agrees well with our observations.

4. Conclusions and Summary

[54] We successfully performed an intercomparison experiment between the NCAR C-130 airborne measurements and four ground-based lidars in the vicinity of Tokyo on 23 April 2001 during the ACE-Asia IOP. A moderate dust layer extending up to 8 km was recognized using the lidars' total depolarization ratio. In the backscattering coefficient at 532 nm, we found a good agreement among lidars' and in situ observations. The intercomparison suggested the mesoscale variability of aerosol concentration as follows. The aerosol layer between 1.6 km and 3.5 km was extremely stable and horizontally homogeneous. The higher variability below 1.6 km can be explained by the difference of PBL height and local surface influence. The higher variability above 3.5 km might be caused by wind sheer due to gravity waves.

[55] The extinction profiles determined by in situ instruments and a tracking Sun photometer also agree well with the profiles estimated from the lidar backscattering profiles above PBL. The lidar profile revealed a close relationship between the altitude variations of the backscattering coefficient and the aerosol depolarization ratio. On the basis of these data it seems probable that there was fine-mode
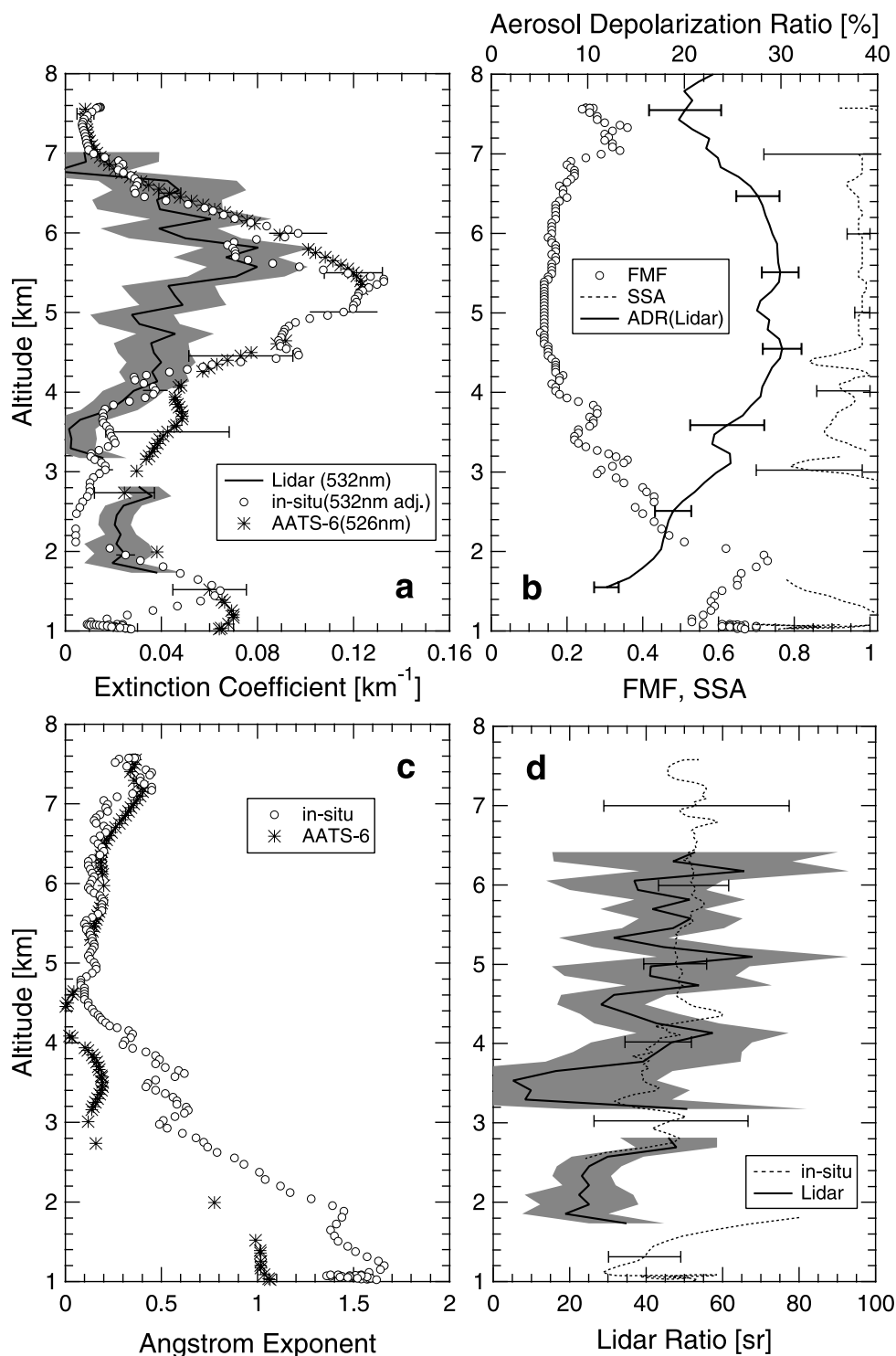
Figure 13. Aerosol optical properties profiled by the airborne in situ tracking Sun photometer measurements in the descending flight during 0732–0806 UTC on 23 April 2001 over around Okayama (133.4°N, 34.5°E) and Raman lidar observation at TUMM in Tokyo during 1011–1302 UTC at night. (a) Extinction coefficient from the in situ, AATS-6, TUMM Raman lidar measurements. (b) Fine mode fraction (FMF) of light scattering, single scattering albedo (SSA) at 550 nm from in situ measurements, and the aerosol depolarization ratio at 532 nm from the lidar. (c) Ångström exponent from the nephelometer and AATS-6. (d) Lidar ratio at 532 nm from the in situ and Raman lidar measurements. Half-tone areas indicate the error bars associated with the lidar data.

dominated aerosol in the boundary layer ($<\sim$1.2 km), fine and coarse (dust) mixed aerosol at intermediate altitudes, and dust dominated aerosol in the higher troposphere ($>$3.5 km).

[56]   Using airborne physical and chemical measurements of the aerosol (i.e., nephelometers, absorption photometer, Sun photometer, optical particle counter, rapid ion chromatography, and SO_2 measurement), we were able to confirm that the observed variations in δ_a were due to a vertical change in the mixing ratio of fine and dust aerosols. We found that δ_a was high ($\sim$30%) and almost constant in the dry and dust-dominated upper layer. In contrast, in the humid and accumulation mode dominated layer, the backscattering coefficient was high and the δ_a was small ($<$10%). At intermediate altitudes, where fine and dust aerosols were "externally" mixed, the increase of fine-mode aerosol scattering raised the backscattering efficiently, which simultaneously lowered the depolarization ratio, and so there was a negative correlation between β_a and δ_a.

[57]   Since similar relationship has often been observed in Tokyo during spring [*Murayama et al.*, 2001a, 2001b] and a similar observation by Raman lidar and airborne measurements in the free troposphere was reported over central Japan [*Sakai et al.*, 2003], we can expect that such a phenomenon is commonly observed over Japan and is associated with the height stratification of fine and dust aerosols [*Hayasaka et al.*, 1990]. Inspection of the mixing state of fine and dust aerosols by looking at the relation between β_a and δ_a should give insight regarding the evolution of dust plumes [e.g., *Zhang and Carmichael*, 1999].

[58]   Using submicron Ca^{2+} as a good indicator of the presence of mineral dust, the chemical data from the C-130 showed that the high depolarization ratio in the free troposphere was indeed due to mineral dust. It is interesting that there was some sulfate even in the dust-dominated layer. This may have arisen from externally mixed sulfate or from $CaSO_4$ as part of the dust. An elevated SO_2 concentration of 10-ppb in the upper PBL suggests the influence of the volcanic plume from Mt. Oyama on Miyake-jima Island.

[59]   In contrast to the large vertical variation of the aerosol size distribution and chemical composition, the lidar ratio was much less height-dependent. The column-averaged in situ lidar ratio was 44.9 $\pm$ 10.9 sr, which agreed well with the value estimated by combining the Mie lidar data with Sun photometer observations.

[60]   The C-130 observed a significant dust layer between 4 and 7 km when it returned to Iwakuni base early in the evening. We compared these observations with Raman lidar observations of the elevated dust layer located at the same altitude later that night. Synoptic and meteorological analyses suggest that we observed dust originating from identical dust storms. The Raman lidar-derived lidar ratio for the center (4.5 to 6.5 km) of the elevated dust layer was 46.5 $\pm$ 10.5 sr, which agrees well with the airborne in situ measurement of 50.4 $\pm$ 9.4 sr in the same height range. The aerosol depolarization ratio of the dust layer was 30% at maximum. These values also agreed well with reported values on the same event observed at Tsukuba [*Sakai et al.*, 2002] and previous lidar observations [*Liu et al.*, 2002; *Murayama*, 2002].

References

Ackermann, J., The extinction-to-backscatter ratio of tropospheric aerosol: A numerical study, *J. Atmos. Oceanic. Technol.*, *15*, 1043–1050, 1998.

Adachi, H., T. Shibata, Y. Iwasaka, and M. Fujiwara, Calibration method for the lidar-observed stratospheric depolarization ratio in the presence of liquid aerosol particles, *Appl. Opt.*, *40*, 6587–6595, 2001.

Anderson, T. L., S. J. Masonis, D. S. Covert, and R. J. Charlson, In situ measurement of the aerosol extinction-to-backscatter ratio at a polluted continental site, *J. Geophys. Res.*, *105*(D22), 26,907–26,915, 2000.

Anderson, T., S. J. Masonis, D. S. Covert, N. Ahlquist, S. Howell, A. D. Clarke, and C. McNaughton, Variability of aerosol optical properties derived from in situ aircraft measurements during ACE-Asia, *J. Geophys. Res.*, *108*(D23), 8647, doi:10.1029/2002JD003247, in press, 2003.

Ångström, A., On the atmospheric transmission of Sun radiation and on dust in the air, *Geogr. Ann.*, *12*, 130–159, 1929.

Ansmann, A., M. Riebesell, U. Wandinger, C. Weitkamp, E. Voss, W. Lahmann, and W. Michaelis, Combined Raman elastic-backscatter LIDAR for vertical profiling of moisture, aerosol extinction, backscatter, and lidar ratio, *Appl. Phys. B*, *55*, 18–28, 1992.

Ansmann, A., F. Wagner, D. Althausen, D. Müller, A. Herber, and U. Wandinger, European pollution aerosol plumes observed with Raman lidar at the Portuguese coast, *J. Geophys. Res.*, *106*(D18), 20,725–20,733, 2001.

Ansmann, A., U. Wandinger, A. Wiedensohler, and U. Leiterer, Lindenberg Aerosol Characterization Experiment 1998 (LACE 98): Overview, *J. Geophys. Res.*, *107*(D21), 8129, doi:10.1029/2000JD000233, 2002.

Behrendt, A., and T. Nakamura, Calculation of the calibration constant of polarization lidar and its dependency on atmospheric temperature, *Opt. Exp.*, *10*, 805–817, 2002.

Biele, J., G. Beyerle, and G. Baumgarten, Polarization lidar: Corrections of instrumental effects, *Opt. Exp.*, *7*, 427–435, 2000.

Charlson, R. J., S. E. Schwartz, J. M. Hales, R. D. Cess, J. A. Coakley Jr., J. E. Hansen, and D. J. Hofmann, Climate forcing by anthropogenic aerosols, *Science*, *255*, 423–430, 1992.

Doherty, S. J., T. L. Anderson, and R. J. Charlson, Measurement of the lidar ratio for atmospheric aerosols with 180° backscatter nephelometer, *Appl. Opt.*, *38*, 1823–1832, 1999.

Fernald, G. F., Analysis of atmospheric lidar observations: Some comments, *Appl. Opt.*, *23*, 652–653, 1984.

Ferrare, R. A., S. H. Melfi, D. N. Whiteman, K. D. Evans, and R. Leifer, Raman lidar measurements of aerosol extinction and backscattering: 1. Methods and comparisons, *J. Geophys. Res.*, *103*(D16), 19,663–19,672, 1998.

Ferrare, R., et al., Comparison of aerosol properties and water vapor among ground and airborne lidars and Sun photometers during TARFOX, *J. Geophys. Res.*, *105*, 9917–9933, 2000.

Ferrare, R. A., D. D. Turner, L. A. Heilman, W. Feltz, O. Dubovik, and T. Tooman, Raman lidar measurements of the aerosol extinction-to-backscatter ratio over the southern Great Plains, *J. Geophys. Res.*, *106*, 20,333–20,347, 2001.

Fiebig, M., A. Petzold, U. Wandinger, M. Wendisch, C. Kiemle, A. Stifter, M. Ebert, T. Rother, and U. Leiterer, Optical closure for an aerosol column: Method, accuracy, and inferable properties applied to a biomass-burning aerosol and its radiative forcing, *J. Geophys. Res.*, *107*(8130), doi:10.1029/2000JD000192, 2002.

Franke, K., A. Ansmann, D. Müller, D. Althausen, F. Wanger, and R. Scheele, One-year observations of particle lidar ratio over the tropical Indian Ocean with Raman lidar, *Geophys. Res. Lett.*, *28*, 4559–4562, 2001.

Hansen, J., M. Sato, and R. Ruedy, Radiative Forcing and climate response, *J. Geophys. Res.*, *102*(D6), 6831–6864, 1997.

Hayasaka, T., T. Nakajima, and M. Tanaka, The coarse particle aerosols in the free troposphere around Japan, *J. Geophys. Res.*, *95*(D9), 14,039–14,047, 1990.

Holben, B. N., et al., AERONET—A federated instrument network and data archive for aerosol characterization, *Remote Sens. Environ.*, *66*, 1–16, 1998.

Huebert, B. J., T. Bates, P. B. Russell, G. Shi, Y. J. Kim, K. Kawamura, G. Carmichael, and T. Nakajima, An overview of ACE-Asia: Strategies for quantifying the relationships between Asian aerosols and their climatic impacts, *J. Geophys. Res.*, *108*(D23), 8633, doi:10.1029/2003JD003550, in press, 2003.

Intergovernmental Panel on Climate Change (IPCC), *Climate Change 2001: The Scientific Basis*, 896 pp., Cambridge Univ. Press, New York, 2001.

Iwasaka, Y., M. Yamato, R. Imasu, and A. Ono, Transport of Asian dust (KOSA) particles: Importance of weak KOSA events on the geochemical cycle of soil particles, *Tellus, Ser. B*, 40, 494–503, 1988.

Kasten, R., Visibility in the prephase of condensation, *Tellus*, 21, 631–635, 1969.

Kaufman, Y. J., et al., Smoke, Clouds, and Radiation-Brazil (SCAR-B) experiment, *J. Geophys. Res.*, 103(D24), 31,783–31,808, 1998.

Kinjo, H., H. Kuze, T. Takamura, and N. Takeuchi, Determination of aerosol extinction-to-backscattering ratio from multiwavelength lidar observation, *Jpn. J. Appl. Phys.*, 40, 434–440, 2001.

Klett, J. D., Lidar inversion with variable backscatter/extinction ratios, *App. Opt.*, 24, 1638–1643, 1985.

Lafleur, B. G., A low turbulence inlet for airborne aerosol sampling, MS thesis, Univ. of Denver, Denver, Colo., 1998.

Liu, Z., N. Sugimoto, and T. Murayama, Extinction-to-backscatter ratio of Asian dust observed with high-spectral-resolution lidar and Raman lidar, *Appl. Opt.*, 41, 2760–2767, 2002.

Masonis, S. J., K. Franke, A. Ansmann, D. Müller, D. Althausen, J. A. Ogren, A. Jefferson, and P. J. Sheridan, An intercomparison of aerosol light extinction and 180° backscatter as derived using in situ instruments and Raman lidar during the INDOEX field campaign, *J. Geophys. Res.*, 107(D19), 8014, doi:10.1029/2000JD000035, 2002.

Measures, R. M., *Laser Remote Sensing*, 510 pp., John Wiley, Hoboken, N. J., 1984.

Mishchenko, M. I., and K. Sassen, Depolarization of lidar returns by small ice crystals: An application to contrails, *Geophys. Res. Lett.*, 25, 309–312, 1998.

Murayama, T., Optical properties of Asian dust aerosol lofted over Tokyo observed by Raman lidar, in *Lidar Remote Sensing in Atmospheric and Earth Sciences, Proceedings of the 21st ILRC*, edited by L. R. Bissonnette, G. Roy, and G. Vallée, pp. 331–334, Defense R&D Canada, Valcartier, Québec, 2002.

Murayama, T., H. Okamoto, N. Kaneyasu, H. Kamataki, and K. Miura, Application of lidar depolarization measurement in the atmospheric boundary layer: Effects of dust and sea-salt particles, *J. Geophys. Res.*, 104(D24), 31,781–31,792, 1999.

Murayama, T., et al., Ground-based network observation of Asian dust events of April 1998 in east Asia, *J. Geophys. Res.*, 106(D16), 18,345–18,359, 2001a.

Murayama, T., et al., Lidar network observation of Asian dust, in *Advances in Laser Remote Sensing, Selected Papers Presented at the 20th ILRC*, edited by A. Dabas, C. Loth, and J. Pelon, pp. 169–172, Ecole Polytech., Paris, 2001b.

Nakajima, T., G. Tonna, R. Rao, P. Boi, Y. Kaufman, and B. Holben, Use of sky brightness measurements from ground for remote sensing of particle polydispersions, *Appl. Opt.*, 35, 2672–2686, 1996.

Raes, F., T. Bates, G. Verver, D. Vogelenzang, and M. Van Liedekerke, The second Aerosol Characterization Experiment (ACE-2), Introduction, meteorological overview, and main results, *Tellus, Ser. B*, 52, 111–126, 1999.

Ramanathan, V., et al., Indian Ocean Experiment: An integrated analysis of the climate forcing and effects of the great Indo-Asian haze, *J. Geophys. Res.*, 106(D22), 28,371–28,398, 2001.

Redemann, J., R. P. Turco, R. F. Pueschel, M. A. Fenn, E. V. Browell, and W. B. Grant, A multi-instrument approach for characterizing the vertical structure of aerosol properties: Case studies in the Pacific Basin troposphere, *J. Geophys. Res.*, 103, 23,287–23,298, 1998.

Redemann, J., et al., Retrieving the vertical structure of the effective aerosol complex index of refraction from a combination of aerosol in situ and remote sensing measurements during TAFROX, *J. Geophys. Res.*, 105, 9949–9970, 2000.

Redemann, J. S., J. Masonis, B. Schmid, T. L. Anderson, P. B. Russell, J. M. Livingston, O. Dubovik, and A. D. Clarke, Clear-column closure studies of aerosols and water vapor aboard the NCAR C-130 in ACE-Asia, 2001, *J. Geophys. Res.*, 108(D23), 8655, doi:10.1029/2003JD003442, in press, 2003.

Russell, P. B., et al., Pinatubo and pre-Pinatubo optical-depth spectra: Mauna Loa measurements, comparisons, inferred particle size distributions, radiative effects, and relationship to lidar data, *J. Geophys. Res.*, 98, 22,969–22,985, 1993.

Russell, P. B., P. V. Hobbs, and L. L. Stowe, Aerosol properties and radiative effects in the U.S. mid-Atlantic haze plume: An overview of the Tropospheric Aerosol Radiative Forcing Observational Experiment (TARFOX), *J. Geophys. Res.*, 104, 2213–2222, 1999.

Sakai, T., et al., Case study of Raman lidar measurements of Asian dust events in 2000 and 2001 at Nagoya and Tsukuba, Japan, *Atmos. Environ.*, 36, 5479–5489, 2002.

Sakai, T., T. Shibata, K. Hara, M. Kido, K. Osada, M. Hayashi, K. Matsunaga, and Y. Iwasaka, Raman lidar and aircraft measurements of tropospheric aerosol particles during the Asian dust event over central Japan: Case study on 23 April 1996, *J. Geophys. Res.*, 108(D12), 4349, doi:10.1029/2002JD003150, 2003.

Sasano, Y., E. V. Browell, and S. Ismail, Error caused by using constant extinction/backscattering ratio in the lidar solution, *Appl. Opt.*, 24, 3929–3932, 1985.

Sassen, K., The lidar backscattering depolarization technique for cloud and aerosol research, in *Light Scattering by Nonspherical Particles: Theory, Measurements, and Geophysical Applications*, edited by M. L. Mishchenko, J. W. Hovenier, and L. D. Travis, pp. 393–416, Academic, San Diego, Calif., 1999.

Schmid, B., et al., Coordinated airborne, spaceborne, and ground-based measurements of massive thick aerosol layers during the dry season in southern Africa, *J. Geophys. Res.*, 108(D13), 8496, doi:10.1029/2002JD002297, 2003.

Swap, R. J., et al., The Southern African Regional Science Initiative (SAFARI 2000), Dry-season field campaign: An overview, *S. Afr. J. Sci.*, 98, 126–130, 2002.

Thornton, D. C., A. R. Bandy, F. H. Tu, B. W. Blomquist, G. M. Mitchell, W. Nadler, and D. H. Lenschow, Fast airborne sulfur dioxide measurements by Atmospheric Pressure Ionization Mass Spectrometry (APIMS), *J. Geophys. Res.*, 107(D22), 4632, doi:10.1029/2002JD002289, 2002.

Wandinger, U., et al., Optical and microphysical characterization of biomass-burning and industrial-pollution aerosols from multiwavelength lidar and aircraft measurements, *J. Geophys. Res.*, 107(D21), 8125, doi:10.1029/2000JD000202, 2002.

Weber, R. J., D. Orsini, Y. Duan, Y.-N. Lee, P. J. Klotz, and F. Brechtel, A particle-into-liquid collector for rapid measurement of aerosol bulk chemical composition, *Aerosol Sci. Technol.*, 35, 718–727, 2001.

Welton, E. J., et al., Ground-based lidar measurements of aerosols during ACE-2: Instrument description, results, and comparisons with other ground-based and airborne measurements, *Tellus, Ser. B*, 52, 636–651, 2000.

Whiteman, D. N., S. H. Melfi, and R. A. Ferrare, Raman lidar system for the measurement of water vapor and aerosols in the Earth's atmosphere, *Appl. Opt.*, 31, 3068–3082, 1992.

Zhang, Y., and G. R. Carmichael, The role of mineral aerosol in tropospheric chemistry in east Asia—A model study, *J. Appl. Meteorol.*, 38, 353–366, 1999.

————————

M. Abo, Department of Electrical Engineering, Tokyo Metropolitan University, 1-1 Mimami-Osawa, Hachioji, Tokyo 192-0397, Japan. (abo@eei.metro-u.ac.jp)

T. L. Anderson and S. J. Masonis, Department of Atmospheric Sciences, University of Washington, Box 351640, 408 ATG, Seattle, WA 98195-1640, USA. (tadand@atmos.washington.edu; sarahd@atmos.washington.edu)

A. Bandy and D. Thornton, Department of Chemistry, Drexel University, Philadelphia, PA 19104, USA. (bandyar@drexel.edu; dct@drexel.edu)

B. Blomquist, A. Clarke, S. G. Howell, B. Huebert, and C. S. McNaughton, Department of Oceanography, University of Hawaii, 1000 Pope Rd., Honolulu, HI 96822, USA. (blomquis@hawaii.edu; tclarke@soest.hawaii.edu; showell@soest.hawaii.edu; huebert@hawaii.edu; cameronm@soest.hawaii.edu)

S. Fukagawa and H. Kuze, Center for Environmental Remote Sensing, Chiba University, 1-33 Yayoi, Inage, Chiba 263-8522, Japan. (shun@ceres.cr.chiba-u.ac.jp; hkuze@ceres.cr.chiba-u.ac.jp)

J. M. Livingston, SRI International, 333 Ravenswood Avenue, Menlo Park, CA 94025, USA. (jlivingston@mail.arc.nasa.gov)

K. Maxwell-Meier, D. A. Orsini, and R. J. Weber, School of Earth and Atmospheric Sciences, Georgia Institute of Technology, Atlanta, GA 30332-0340, USA. (kmaxwell@eas.gatech.edu; douglas.orsini@eas.gatech.edu; rweber@eas.gatech.edu)

T. Murayama, Tokyo University of Mercantile Marine, 2-1-6 Etchujima, Koto, Tokyo 135-8533, Japan. (murayama@ipc.tosho-u.ac.jp)

J. Redemann and B. Schmid, Bay Area Environmental Research Institute, 560 3rd Street, Sonoma, CA 95476, USA. (jredemann@mail.arc.nasa.gov; bschmid@mail.arc.nasa.gov)

P. B. Russell, NASA Ames Research Center, Moffett Field, CA 94035-1000, USA. (prussell@mail.arc.nasa.gov)

A. Shimizu and N. Sugimoto, Atmospheric Environment Division, National Institute of Environmental Studies, 6-2 Onogawa, Tsukuba 305-8506, Japan. (shimizua@nies.go.jp; nsugimot@nies.go.jp)
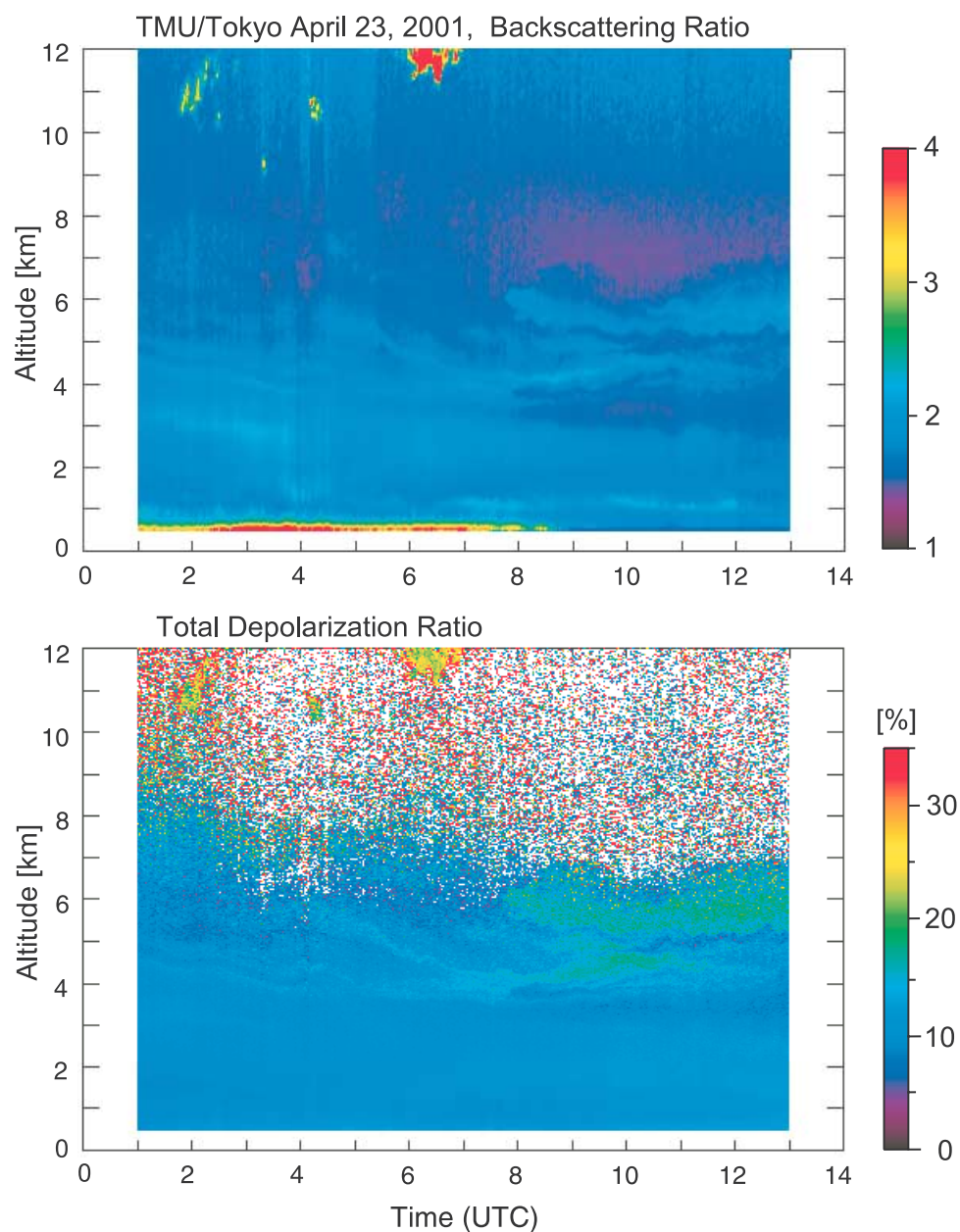
M. Yabuki, National Institute of Polar Research, 1-9-10 Kaga, Itabashi, Tokyo 173-8515, Japan. (yabuki@pmg.nipr.ac.jp)
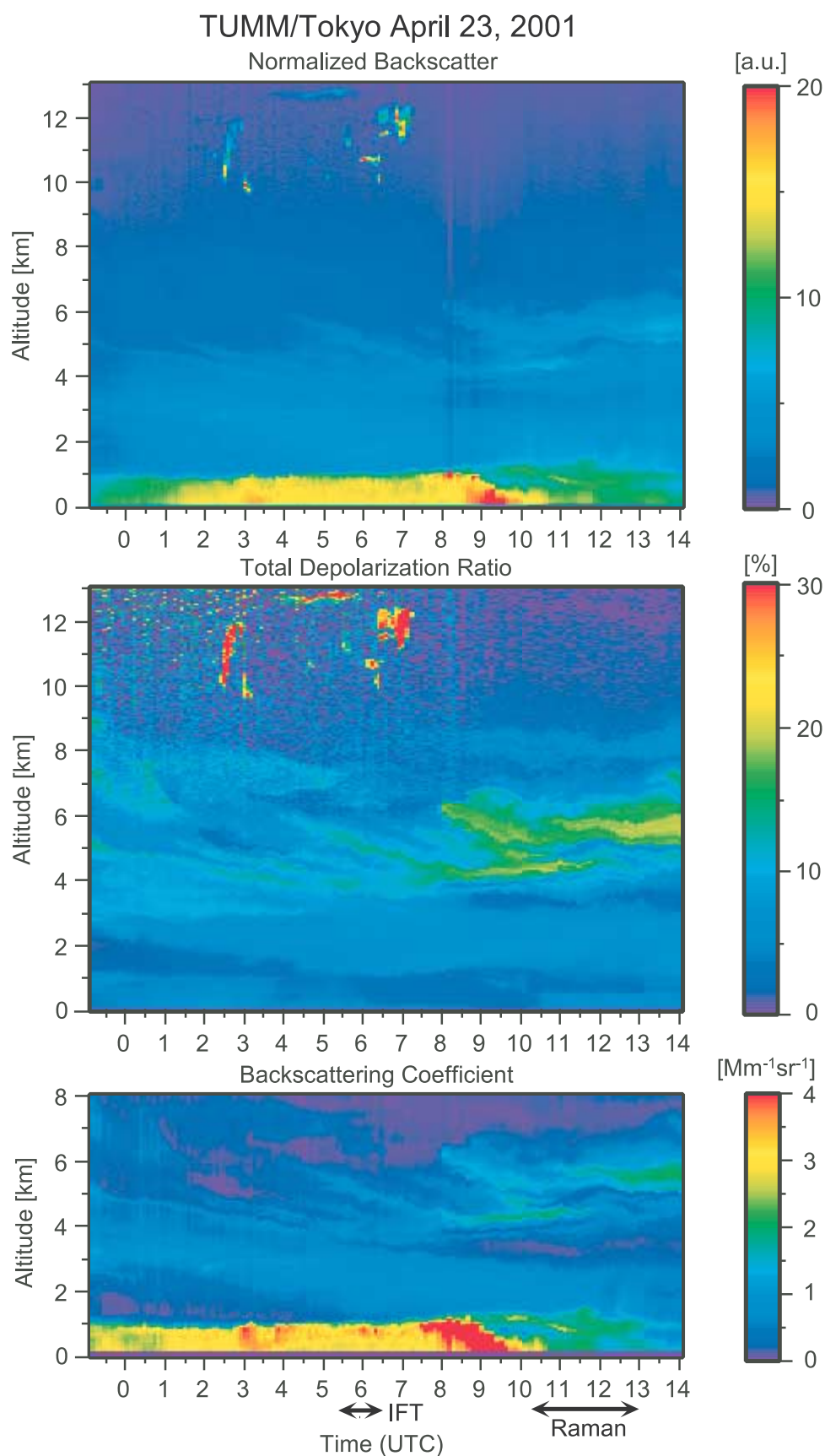
Figure 4. (top) Time-to-height indications of the normalized backscatter signal, (middle) the total depolarization ratio, and (bottom) the backscattering coefficient at 532 nm in TUMM on 23 April 2001. Arrows indicates the time period of the intercomparison flight and Raman-lidar mode observations.

Figure 5. (top) THIs of the backscattering ratio and (bottom) the total depolarization ratio at 532 nm in TMU on 23 April 2001. Although TMU locates about 50 km west of TUMM, the both data agree well each other except in the boundary layer.